Tracking the Metal-Centered Triplet in Photoinduced Spin Crossover of $Fe(phen)_3^{2+}$ with Tabletop Femtosecond M-edge XANES

Kaili Zhang†, Ryan Ash†, Gregory S. Girolami, Josh Vura-Weis*

Department of Chemistry, University of Illinois at Urbana-Champaign, Urbana, Illinois 61801, United States

Abstract: Fe(II) coordination complexes are promising alternatives to Ru(II) and Ir(III) chromophores for photoredox chemistry and solar energy conversion, but rapid deactivation of the initial metal-to-ligand charge transfer (MLCT) state to low-lying (d,d) states limits their performance. Relaxation to a long-lived quintet state is postulated to occur via a metal-centered triplet state, but this mechanism remains controversial. We use femtosecond extreme ultraviolet (XUV) transient absorption spectroscopy to measure the excited-state relaxation of $Fe(phen)_3^{2+}$ and conclusively identify a ^3T intermediate that forms in 170 fs and decays to a vibrationally hot $^5T_{2g}$ state in 40 fs. A coherent vibrational wavepacket with a period of 250 fs and damping time of 0.66 ps is observed on the $^5T_{2g}$ surface, and the spectrum of this oscillation serves as a fingerprint for the Fe-N symmetric stretch. The results show that the shape of the $M_{2,3}$-edge X-ray absorption near edge structure (XANES) spectrum is sensitive to the electronic structure of the metal center, and the high spin sensitivity, fast time resolution, and tabletop convenience of XUV transient absorption make it a powerful tool for studying the complex photophysics of transition metal complexes.

Introduction

In the past several years there has been a surge of interest in Fe^{II} polypyridyl complexes as chromophores for photocatalytic and photovoltaic applications, with the aim of replacing expensive Ru^{II} and Ir^{III} photosensitizers.[1–4] This goal is challenging because the weaker ligand field of first-row transition metals creates a cascade of low-lying metal-centered states that rapidly deactivate the initial excited state. For example, both $Ru(bpy)_3^{2+}$ (bpy = 2,2'-bipyridine) and $Fe(bpy)_3^{2+}$ have metal-to-ligand charge transfer (MLCT) states that lie 2 to 3 eV above the ground state. However, the MLCT state of $Ru(bpy)_3^{2+}$ has a lifetime of hundreds of nanoseconds whereas that of $Fe(bpy)_3^{2+}$ decays within 200 fs into a low-energy $^5T_{2g}$ state with 100% quantum yield. Consequently, the energy is wasted as molecular vibrations long before any useful photochemistry can occur. Chemists have tackled this challenge by engineering molecules that either raise the energy of the metal-centered excited states above the energy of the MLCT state (a thermodynamic solution) or displace/deform the excited-state potential energy surfaces of the metal-centered states to trap molecules in high-energy metastable MLCT or triplet metal-centered states (a kinetic solution).[3] These strategies have had some success: Fe^{II} complexes with excited-state lifetimes as long as 528 ps have been described.[5]

Despite these advances, there is still considerable uncertainty about the excited-state dynamics of Fe^{II} polypyridyl molecules, due to the complex interplay between electronic, spin, and nuclear degrees of freedom. It has long been speculated that conversion of the MLCT state to the $^5T_{2g}$ state occurs via a triplet metal-centered excited state ($^3T_{2g}$ or $^3T_{1g}$), but the role of this triplet remains controversial. Because the spin transition occurs in a region of the potential energy surface with curve crossings between multiplet states, the formation of a triplet intermediate cannot be ruled out on theoretical grounds.[6,7] In addition, the formation of ^3T states cannot easily be probed by conventional visible-light transient absorption methods, because the d-d transitions are weak compared to the intense MLCT

band. As a result, the spectra are relatively insensitive to the spin state of the metal center.

Other spectroscopic techniques have afforded conflicting information about whether triplet states are generated upon excitation of Fe^{II} polypyridyl complexes. By using the spin-selective technique of femtosecond Fe K_β emission at a free-electron laser, Zhang et al. identified a spectroscopic signature consistent with formation of a triplet intermediate in $Fe(bpy)_3^{2+}$.[8] However, Auböck and Chergui used femtosecond ultraviolet transient absorption spectroscopy to show that $Fe(bpy)_3^{2+}$ converts into a vibrationally hot $^5T_{2g}$ state within 50 fs; these authors argued that this time scale was too short to admit a triplet intermediate.[9] More recently, Lemke et al. carried out ultrafast Fe K-edge X-ray absorption studies of $Fe(bpy)_3^{2+}$ and concluded that the time-dependent spectra are consistent with formation of a triplet intermediate.[10] Slow progress in the detection of these short-lived excited states can be ascribed in part to the scarce beamtime available at X-ray free-electron laser facilities capable of performing femtosecond spin-selective spectroscopy.

In this work, we use tabletop femtosecond extreme ultraviolet (XUV) transient absorption spectroscopy to provide direct and unambiguous evidence that a metal-centered triplet intermediate is generated following MLCT excitation of the Fe^{II} o-phenanthroline complex $Fe(phen)_3^{2+}$. We also find that a coherent vibrational wavepacket on the $^5T_{2g}$ surface leads to an oscillation in the transient spectrum that corresponds to the Fe-N symmetric stretch. Ligand field multiplet simulations confirm these assignments. These results illustrate the utility and power of X-ray absorption near edge structure (XANES) spectroscopy at the Fe $M_{2,3}$-edge, a technique that is sensitive to the oxidation state and spin-state of the metal center as well as the ligand field symmetry and strength.[11–15]

Experimental

XUV Transient Absorption: The XUV probe is produced by high harmonic generation using a tabletop instrument described previously.[11,16] Briefly, a Ti:sapphire driving laser (800 nm, 4 mJ, 35 fs, 1 kHz) is focused into a semi-infinite gas cell filled with 120 Torr of neon, where the intense electric field at the focal point generates a ~15 fs XUV pulse with a broad spectrum spanning 50 to 90 eV. Residual driving laser photons are attenuated by a Si mirror and a 100 nm thick Al filter. XUV photons are collected in transmission mode and dispersed by a diffraction grating onto an array CCD detector. The spectrometer resolution is 0.6 eV FWHM as measured from the atomic absorption lines of Xe. A secondary output from the driving laser is sent through a non-collinear optical parametric amplifier (TOPAS-White) to generate the pump pulse (35 fs, 535 nm). The instrument response time is 40 fs FWHM, as determined by measuring the rise of α-Fe_2O_3 transient absorption features.[13,17] Samples were deposited as ~100 nm thick films on Si_3N_4 substrates. Further experimental details can be found in Sections S1 and S3 of the Supporting Information.

Ligand-field multiplet theory simulations: The procedure for computing LFM theory simulations of $M_{2,3}$-edge spectra of metal-centered excited states using a modified version of the program CTM4XAS has been described in a previous publication.[14] Briefly, the metal center is modeled in terms of a parametric Hamiltonian containing electron-nuclear and electron-electron Coulombic interactions, spin-orbit coupling and an electrostatic crystal field.[18,19] The parameters used in the present study can be found in section S7 of the Supporting Information. The identities of the eigenstates of the Hamiltonian are assigned by expanding the spin-orbit coupled states in terms of pure-spin basis functions. $M_{2,3}$-edge stick spectra are computed between eigenstates of $3p^63d^N$ and $3p^53d^{N+1}$ configurations. Each transition is broadened by a Lorentzian whose width is determined by computing the Auger decay rate of the corresponding $3p^53d^{N+1}$ state. A floor of 1.0 eV is imposed to account for other decay channels. The transitions are further broadened by a Gaussian with σ=0.2 eV to account for finite instrumental resolution.

The simulated spectrum of the $^1A_{1g}$ state of Fe^{II} has been rescaled to 60% of the computed intensity in accordance with the experimentally observed intensity difference in the spectra of the $^1A_{1g}$ and $^5T_{2g}$ states of $Fe[H_2B(pz)_2]_2(bpy)$. Simulated difference spectra of Fe^{II} metal-centered excited states are computed by subtracting the simulated absorption spectrum of the $^1A_{1g}$ state from those of the excited states. The difference spectrum of MLCT excited state is computed as the difference of the simulated spectrum of the $^2T_{2g}$ state of Fe^{III} (rescaled to 60%) minus that of the $^1A_{1g}$ state of Fe^{II}. All spectra are shifted along the energy axis to place the degeneracy-weighted average transition energy at 56.4 eV for the $^1A_{1g}$ state, at 55.2 eV for all Fe^{II} metal-centered excited states and at 56.2 eV for the Fe^{III} $^2T_{2g}$ state.

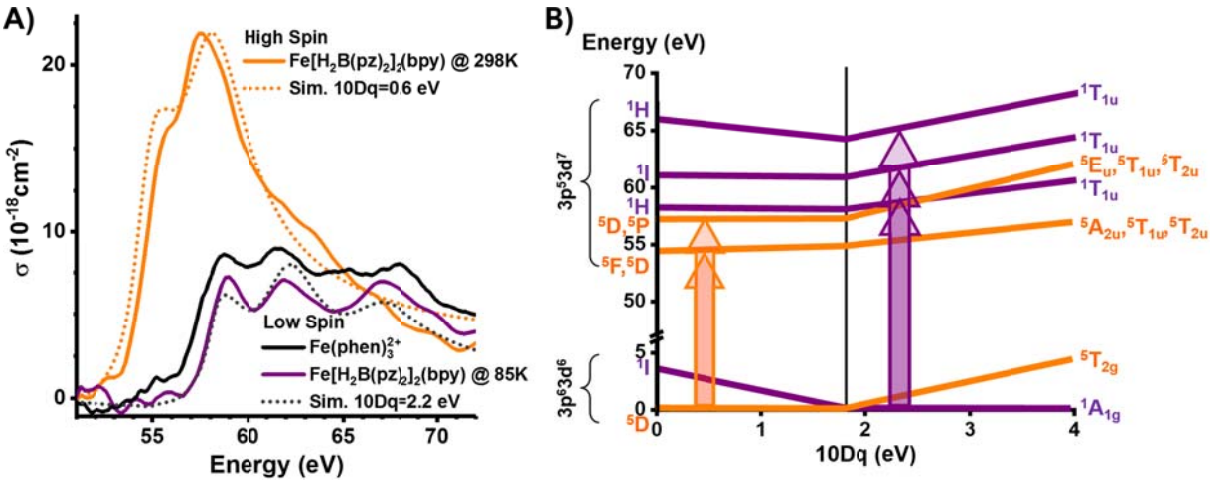

Figure 1: A) Experimental and simulated $M_{2,3}$-edge spectra of high-spin and low-spin Fe^{II} complexes. B) Correlation diagram showing the allowed XUV transitions between the $3p^63d^6$ ground state and the $3p^53d^7$ core-hole excited state as a function of the ligand field strength 10Dq. The break at 1.8 eV is caused by the crossover between a high-spin and low-spin ground state. The effects of spin-orbit coupling are weak and for simplicity are not shown.

Results and Discussion

Ground-State Spectra: XUV spectroscopy is performed using a tabletop laser-based source that produces a broad XUV continuum spanning the range from 50 to 90 eV (see Experimental section). The ground state spectrum of $Fe(phen)_3^{2+}$ is typical of low-spin Fe^{II} complexes,[16] and features three peaks of approximately equal height at 58.7, 61.5, and 68.0 eV (Figure 1). To demonstrate the spin sensitivity of M-edge XANES and to estimate the transient spectrum upon spin crossover, we recorded the temperature-dependent ground-state spectra of the thermal spin crossover complex $Fe[H_2B(pz)_2]_2(bpy)$.[20] This model complex switches from a low-spin singlet to a high-spin quintet at 150 K. As shown in Figure 1A, the low-spin spectrum recorded at 85 K is similar to that of $Fe(phen)_3^{2+}$, with only minimal shifts in the peak positions. The HS spectrum recorded at room temperature is redshifted and approximately three times as intense, with a major peak at 57.5 eV and a shoulder at 55.6 eV. As is commonly observed in L-edge spectroscopy (2p→3d excitation), HS spectra are generally redshifted from their LS analogues due to additional exchange stabilization of the HS core-hole state.[21]

These spectra can be understood with the aid of the correlation diagram in Figure 1B, which is analogous to the Tanabe-Sugano diagrams used to interpret d-d excitations. The XUV probe measures transitions between the $3p^63d^6$ ground state and $3p^53d^7$ core-hole excited states. On the high-spin, weak-field (left) side of this diagram, transitions are allowed from the ^5D-derived ground state to a closely-spaced group of ^5F- and ^5D-derived states at ~55 eV and another group of ^5D- and ^5P-derived states at ~58 eV. On the low-spin, strong-field (right) side of the diagram, the electronic state is better described by Mulliken term symbols within octahedral symmetry. Transitions are allowed between the $^1A_{1g}$ ground state and three $^1T_{1u}$ core-hole states; the transitions appear at approximately 58, 62, and 65 eV. The position of each peak depends on the ligand field splitting 10Dq, making the spectrum a sensitive probe of the ligand field strength. Spin-orbit coupling is included in the actual spectral simulations, but is weak enough to be omitted in this qualitative description.

Transient M-edge XANES and Kinetic Modeling: The femtosecond dynamics of $Fe(phen)_3^{2+}$ were measured by photoexciting the sample at its MLCT band with a 35 fs, 535 nm pump and probing with a 15 fs broadband XUV probe (see Materials and Methods for a detailed description of the instrument). Figure 2A shows a contour plot of the transient absorption spectrum, where $\Delta A = -log_{10}(I_{pump\ on}/I_{pump\ off})$. Spectroscopic slices at selected delay times are shown in Figure 2C. The IRF-limited initial state (as shown by the 30 fs slice) has a weak, broad positive feature between 53 and 62 eV. By 100 fs, a peak rises at 57.0 eV with a shoulder at 61.0 eV and a small isolated peak at 64.0 eV. Over the next ~400 fs the peak at 57.0 eV rises further and develops a clear shoulder at 54.5 eV, and the peak at 64.0 eV disappears. A broad bleach from 65 to 75 eV also appears on this timescale. Beyond 500 fs, the shape of the difference spectrum closely resembles the high-spin/low-spin thermal difference

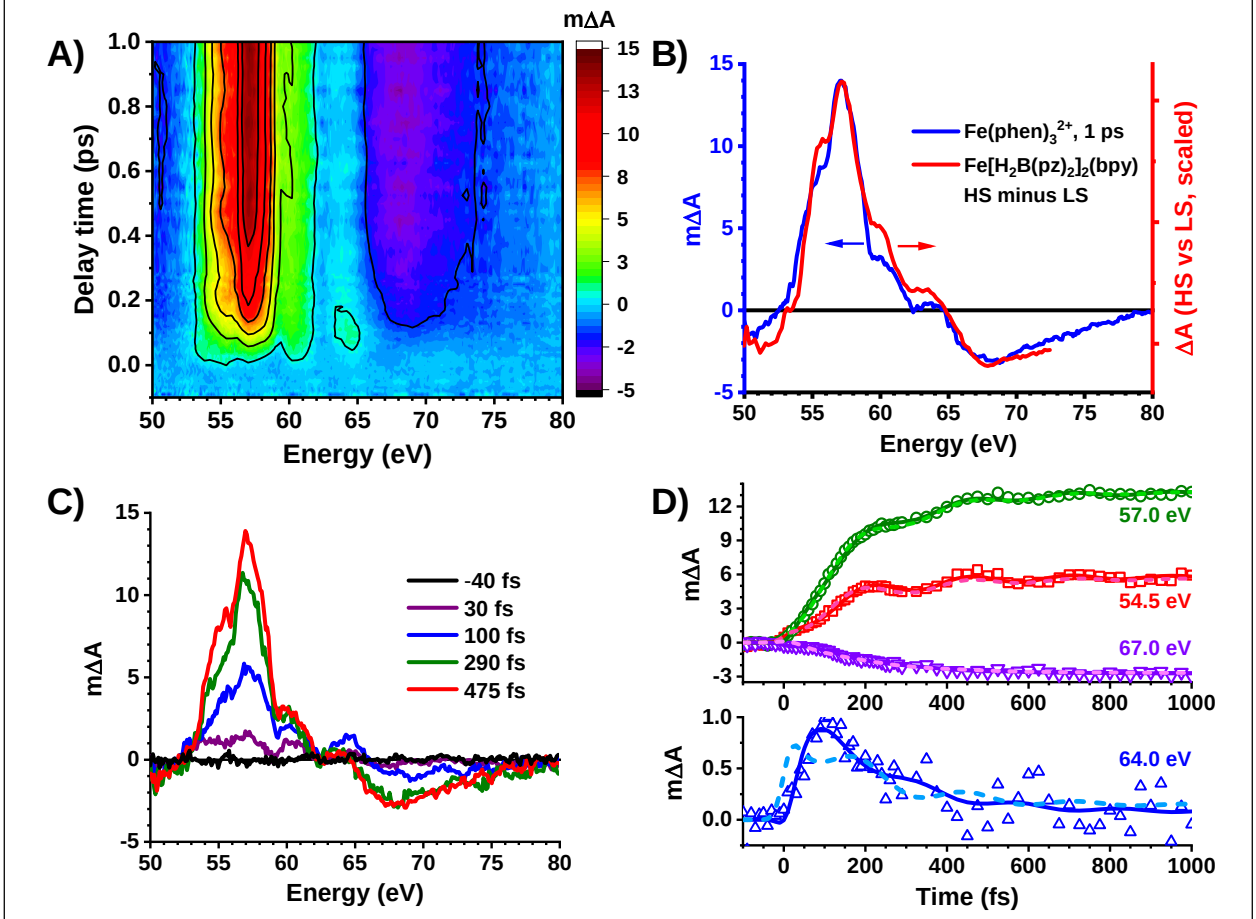

Figure 2: A) Contour plot of transient M-edge XANES spectra of $Fe(phen)_3^{2+}$. B) Transient spectrum of $Fe(phen)_3^{2+}$ at 1 ps compared to the thermal difference spectrum of $Fe[H_2B(pz)_2]_2(bpy)$. C) Transient spectra of $Fe(phen)_3^{2+}$ at selected times. D) Experimental kinetic slices at selected energies (open symbols), with reconstructed kinetics from global fits. Solid lines include the ^3T intermediate, while dashed lines assume the $^5T_2$ state is formed directly from the ^{1,3}MLCT state. The two fits are indistinguishable at 54.5 eV, 57.0 eV, and 67.0 eV, but only the $^{1,3}MLCT \rightarrow {}^3T \rightarrow {}^5T_{2g}$ model successfully fits the data at 64.0 eV.

spectrum (A_{hot} – A_{cold}) of the iron(II) complex $Fe[H_2B(pz)_2]_2(bpy)$ (Figure 2B). This similarity confirms that photoexcitated $Fe(phen)_3^{2+}$ converts into a long-lived high-spin state.

Kinetic slices at select energies are shown in Figure 2D, with the data shown as open symbols; fits with and without the ^3T intermediate (discussed below) are shown as solid and dashed lines, respectively. Both the 57.0 eV peak and 54.5 eV shoulder show clear oscillations with a period of ~250 fs. The relative amplitude of the oscillation is strongest at 54.5 eV, where it is 25% of the average signal. The peak at 64.0 eV rises to a maximum at 90 fs before decaying to near baseline by 400 fs. This rise is considerably delayed compared to the 40 fs FWHM instrumental response function, indicating that this signal is not due to the directly pumped ^{1}MLCT state or the rapidly-formed ^{3}MLCT state.[22] The M-edge XANES spectrum is not sensitive to ferro/antiferromagnetic coupling between the metal and ligand spins, so the singlet and triplet MLCT states are expected to have identical spectra in this energy range.

Two different kinetic models were used to perform global fits of the transient M-edge XANES spectra of $Fe(phen)_3^{2+}$ vs. time: (1) a three-state kinetic model that includes an intermediate (presumably ^3T) state, i.e., $^{1,3}MLCT \xrightarrow{\tau_1} {}^3T \xrightarrow{\tau_2} {}^5T_{2g}$, and (2) a two-state kinetic model that excludes this intermediate state, i.e., $^{1,3}MLCT \xrightarrow{\tau_1} {}^5T_{2g}$. In both models, the final $^5T_{2g}$ state has an additional damped oscillatory component. The process of spin crossover accompanied by vibrational coherence is modeled using a spin-boson

model in which the transitions between electronic states are treated phenomenologically as first-order processes.[7,23] Time zero was determined from concurrently-measured transient absorption spectra of α-Fe_2O_3, which exhibits a IRF-limited population of a ligand to metal charge transfer (LMCT) state.[13] Additional details about the models used here, including explicit expressions of the modeled signal as a function of time, energy, and fit parameters, are included in Section S4 of the supporting information.

Fitting to the three-state model gave decay lifetimes of τ_1 = 169.8 ± 0.5 fs for the ^{1,3}MLCT state and τ_2 = 40.0 ± 0.5 fs for the ^{3}T intermediate. Errors are reported as ±1σ uncertainties of the fit; note that the fit algorithm partitions the uncertainty between the time constants and the spectral components. The MLCT lifetime matches well with the range of reported lifetimes for MLCT states of related systems,[8,10,21,24,25] and τ_2 is in reasonable agreement with the value determined for $Fe(bpy)_3^{2+}$ by Fe K_β-edge emission (70 ± 30 fs).[8]

The period of oscillation of the final $^5T_{2g}$ state is 250 ± 0.3 fs, corresponding to a frequency of 133 ± 0.2 cm^{-1}. This frequency is ~15% higher than that of the 116 cm^{-1} fully symmetric breathing mode of HS $Fe(phen)_3^{2+}$ predicted by density functional theory (DFT) calculations (See supporting information Section S9 for computational details). A difference of a similar magnitude between the observed coherent oscillation frequency and DFT-predicted vibrational

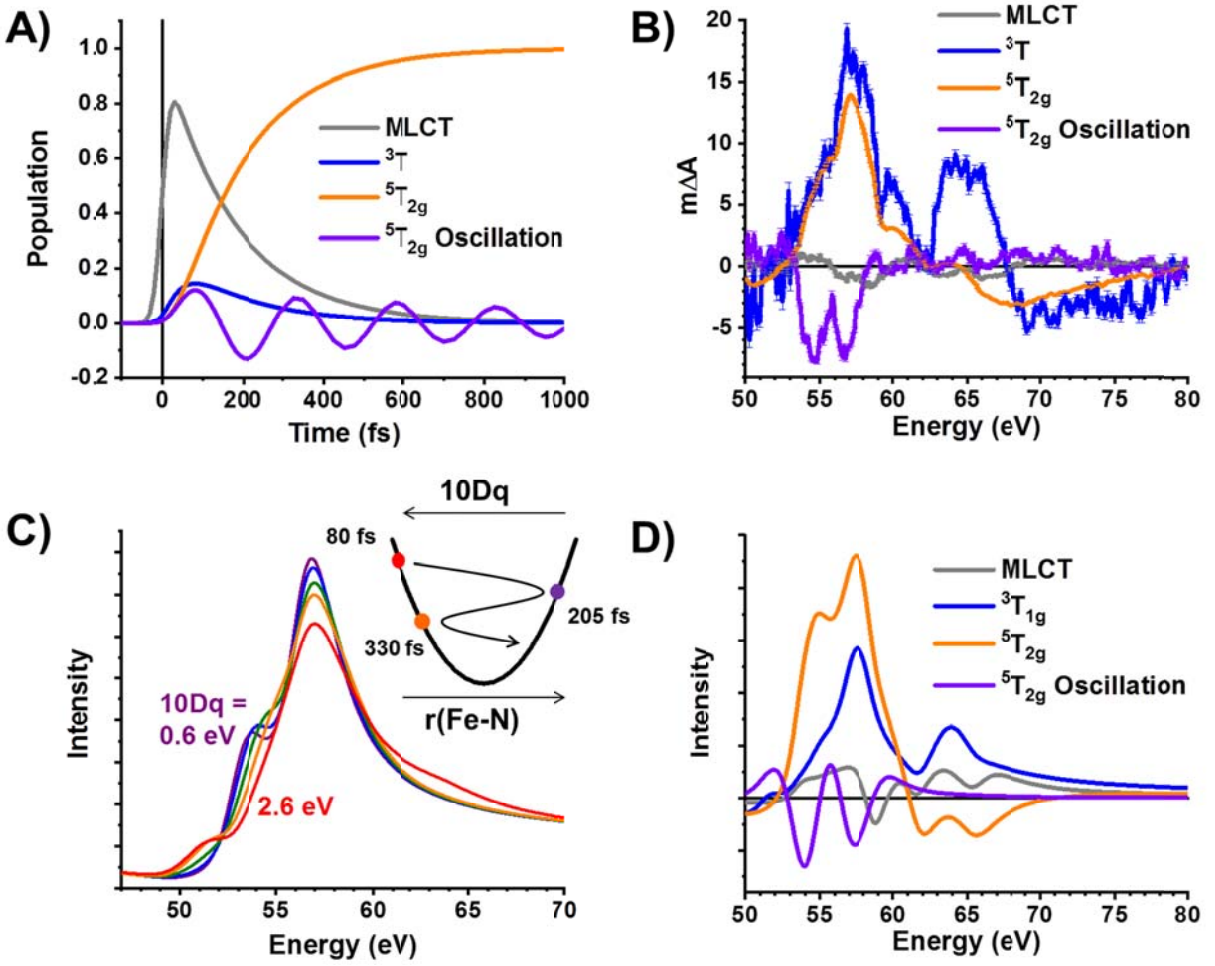

Figure 3 A) Population of each species, and amplitude of the oscillatory component of the $^5T_{2g}$ spectrum, as a function of time. B) Spectral components of the global fit to the ^{1,3}MLCT→^{3}T→$^5T_{2g}$ model. Error bars on the spectra represent ±1σ uncertainty of the fit. C) Ligand field multiplet simulations of the $^5T_{2g}$ state as a function of the ligand field strength 10Dq. The inset shows the coherent oscillation on the $^5T_{2g}$ potential energy surface and the inverse relationship between the Fe-N distance and 10Dq. D) Ligand field multiplet simulations of the transient spectra using the program CTM4XAS. The simulations are excellent qualitative matches for the experimental components in (B), in particular the 64 eV peak indicative of the ^{3}T intermediate.

frequency has been reported for crystalline $Fe(phen)_2(NCS)_2$ (expt. 116 cm^{-1} vs DFT 96 cm^{-1}).[26,27] In both cases, the discrepancies between the computed and experimental frequencies are probably due to solid-state packing effects.

The vibrational coherence of the final $^5T_{2g}$ state has a damping time of 0.66 ± 0.01 ps. The damping rate of vibrational coherence in condensed phases is highly variable. Our value, measured from an amorphous/nanocrystalline sample, falls within the range previously measured from solution samples (e.g., 0.4 – 1 ps depending on wavelength),[9,24] liquid jet samples (320 fs),[10] and crystalline solid samples (0.166 ps)[27] of related compounds. The time-dependent state populations and spectroscopic components obtained from this three-state fit are shown in Figure 3A and B. Reconstructed kinetic traces (Figure 2D) closely match the experimental results.

The two-state model without the ^3T intermediate fits the spectroscopic features at 54.5, 57.0, and 67.0 eV equally well, but the ^3T state is required to reproduce the 64.0 eV feature. For this reason, we will confine the rest of the present discussion to the three-state model with the ^3T intermediate. A detailed discussion of the two-state model is given in Section S6 of the Supporting Information, along with a comparison of the residual from each fit.

Additional information about the species formed upon photoexcitation of $Fe(phen)_3^{2+}$ is provided by the shapes of the spectral components deduced from the fit to the three-state model. As shown in Figure 3B, the spectrum of the MLCT state is quite weak, featuring a slight positive feature between 51 and 55 eV and a slight negative feature between 55 and 60 eV. As discussed in Section S8 of the Supporting Information, the low intensity of this transient spectrum is explained by a coincidental similarity between the $^1A_{1g}$ ground state and Fe^{III} $^2T_{2g}$ MLCT spectra. The fit also shows that the ^3T component has an intense positive feature at 57.0 eV, a shoulder at 60.0 eV, and a strong positive peak between 63 and 67 eV. Finally, the spectrum of the $^5T_{2g}$ component matches the 1 ps spectrum shown in Figure 2B, and the oscillatory component has two negative peaks at 54.7 and 56.8 eV.

These experimental components match ligand field multiplet (LFM) simulations carried out with the program CTM4XAS (Figure 3D). The extracted $^5T_{2g}$ spectrum agrees well with the corresponding simulation, which contains strong positive features at 54.8 and 57.4 eV and a broad bleach from 61-70 eV. The $^3T_{1g}$ simulation has peaks at 57.6 and 63.9 eV, which agree almost exactly with the spectrum of the intermediate deduced from the fit to the three-state model. As shown in Section S7 of the Supporting Information, a simulation of the $^3T_{2g}$ transient spectrum is also a good match to experiment, so this experiment cannot confidently distinguish between the two triplet states. In either case, the experimental spectrum is more intense than what LFM simulations suggest. In view of the rapid excited-state dynamics, which especially in the case of the ^3T intermediate permit only a single passage through the transition state to $^5T_{2g}$, the first-order kinetic model used here will underestimate the population of the intermediate and overestimate its spectral contribution.[28]

As noted above, a vibrational coherence with a period of 250 fs is observed on the $^5T_{2g}$ surface. The spectrum of this oscillation serves as a fingerprint for the structural distortion activated by the spin crossover event. The most prominent structural difference between the Franck-Condon geometry and the relaxed $^5T_{2g}$ geometry is the fully-symmetric expansion of the Fe-N cage, which in the computational framework used here is modeled as a decrease in the ligand field strength 10Dq. As shown in Figure 3C, the intensities of the 54.5 eV shoulder and 57.0 eV peak are inversely correlated with the ligand field strength. Therefore, a vibrational wavepacket launched on the compressed side of the Fe-N potential surface (large 10Dq) will initially have low absorbance at these energies, and the signal at these energies will reach a maximum one half-period later at the outer turning point. This prediction is confirmed by the negative amplitude of the fitted oscillatory component in Figure 3C, which is an excellent match for the simulated component in Figure 3D. Note that the kinetic model used in the fit properly accounts for the phase of the vibrational wavepacket: for example the portion of the $^5T_{2g}$ population that is launched at time t will be out of phase with the portion of the population launched at time (t + 125 fs), and their oscillatory components will cancel via destructive interference. Figure 4 summarizes the full excited-state relaxation dynamics.

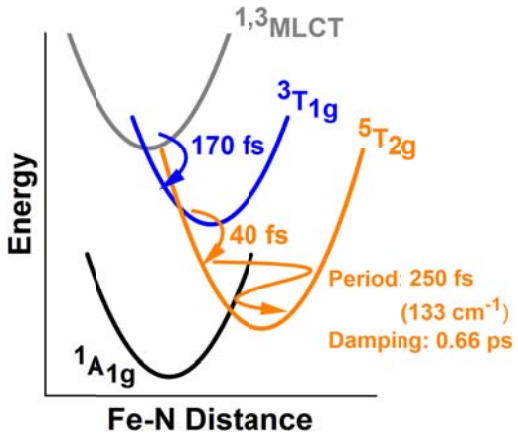

Figure 4: Summary of the excited-state relaxation observed for $Fe(phen)_3^{2+}$.

Prospects for M-edge XANES studies of metal-centered photophysics: Much of the success in designing new Fe^{II} chromophores derives from increased understanding of the excited state potential energy surfaces and their crossing points. Intramolecular vibrational relaxation within each electronic state competes with intersystem crossing between states, so small changes in these surfaces, or in the initial photoexcitation conditions, may lead to large changes in the photophysics. A striking example of this fine-tuning was recently reported by Chábera et al. for the Fe^{II} carbene complex $Fe(btz)_3$, in which the excited-state dynamics depend sensitively on the excitation wavelength.[29] Although excitation of this molecule into high-energy MLCT bands at wavelengths shorter than 690 nm showed a competition between intramolecular vibrational relaxation (IVR) and intersystem crossing (ISC) to a ^{3}MC state, molecules excited into to the lowest MLCT band at 825 nm lack sufficient vibration energy to cross the barrier to the thermodynamically favorable ^{3}MC state. A similar conceptual framework was employed to design an Fe^{III} carbene complex with a 2 ns LMCT lifetime; again the system is kinetically trapped and unable to access a lower-energy metal-centered state.[30]

These conceptual and synthetic advances emerged in parallel with new spectroscopic techniques, from the use of femtosecond visible-light spectroscopy to measure the initial ISC and thermalization of the ^{1,3}MLCT state,[22,31] to the development of X-ray fluorescence as a spin-selective probe of metal-centered states.[32,33] In the work presented here, we establish tabletop femtosecond M-edge XANES as a powerful tool for measuring the ultrafast dynamics of spin crossover. The spin sensitivity of the higher-energy technique of L-edge XANES (2p→3d transitions) has been demonstrated for this class of molecules,[21,34] although a shortage of femtosecond soft X-ray beamlines has made that technique inaccessible to most researchers.

In both M- and L-edge spectroscopy, the strong angular momentum-dependent Coulomb and exchange interactions between the 3p/2p core-hole and the 3d valence electrons lead to qualitatively distinct spectra for different spin states. These clear spectroscopic signatures make identification of intermediate states relatively straightforward. M-edge spectra are especially intuitive and can be described using traditional ligand field theory, and their sensitivity to ligand field strength and symmetry provides a fingerprint for specific normal modes in excited-state vibrational wavepackets.

The 40-fs time resolution in this experiment is readily achievable using modern Ti:sapphire amplifiers, and the in-lab instrument allows state-specific spectroscopy to keep up with new molecular design strategies. One significant limitation of the XUV probe is the short penetration depth, which has so far limited transient absorption spectroscopy to thin-film or gas-phase samples, thus limiting opportunities to study important contributions of solvation.[35] This restriction may soon be lifted by new developments in liquid sheet-jet delivery systems, which have been shown to provide stable, thickness-tunable platforms for spectroscopy in the hard and soft X-ray spectroscopic regions.[36,37]

Conclusion

In this work, we use M-edge XANES spectroscopy to show that photoexcitation of the MLCT transition of $Fe(phen)_3^{2+}$ forms a metastable $^5T_{2g}$ state via a ^{3}T intermediate. This intermediate state is conclusively identified on the basis of ligand field multiplet simulations of the extracted excited state spectrum. We also observed coherent oscillations consistent with vibrational relaxation on the $^5T_{2g}$ potential energy surface, and the spectrum of this oscillation fingerprints the Fe-N symmetric stretch activated by spin crossover. The rich information in $M_{2,3}$-edge XANES, combined with the increasing accessibility of tabletop sources, makes transient studies in the XUV spectral region a powerful tool for resolving ultrafast photophysics of transition metal complexes.

ASSOCIATED CONTENT

Supporting Information

Further information about experimental and computational details. This material is available free of charge via the Internet at http://pubs.acs.org.

AUTHOR INFORMATION

Corresponding Author

*vuraweis@illinois.edu

Author Contributions

†These authors contributed equally to this work

ACKNOWLEDGMENTS

This material is based upon work supported by the National Science Foundation under Grant No. 1555245. The transient XUV instrument, including the nonlinear optical parametric amplifier, was built with funding from the Air Force Office of Scientific Research under AFOSR Award No. FA9550-14-1-0314. GSG acknowledges the support of the William and Janet Lycan Fund at the University of Illinois.

REFERENCES

(1) Abrahamsson, M. Solar Energy Conversion Using Iron Polypyridyl Type Photosensitizers - A Viable Route for the Future? *Photochemistry* **2017**, *44*, 285–295.

(2) Prier, C. K.; Rankic, D. A.; MacMillan, D. W. C. Visible Light Photoredox Catalysis with Transition Metal Complexes: Applications in Organic Synthesis. *Chem. Rev.* **2013**, *113* (7), 5322–5363.

(3) Wenger, O. S. Is Iron the New Ruthenium? *Chem. - A Eur. J.* **2019**, *25* (24), 6043–6052.

(4) McCusker, J. K. Electronic Structure in the Transition Metal Block and Its Implications for Light Harvesting. *Science* **2019**, *363* (6426), 484–488.

(5) Chábera, P.; Kjaer, K. S.; Prakash, O.; Honarfar, A.; Liu, Y.; Fredin, L. A.; Harlang, T. C. B.; Lidin, S.; Uhlig, J.; Sundström, V.; Lomoth, R.; Persson, P.; Wärnmark, K. Fe^{II} Hexa N-Heterocyclic Carbene Complex with a 528 Ps Metal-To-Ligand Charge-Transfer Excited-State Lifetime. *J. Phys. Chem. Lett.* **2018**, *9* (3), 459–463.

(6) Sousa, C.; de Graaf, C.; Rudavskyi, A.; Broer, R.; Tatchen, J.; Etinski, M.; Marian, C. M. Ultrafast Deactivation Mechanism of the Excited Singlet in the Light-Induced Spin Crossover of $[Fe(2,2'\text{-Bipyridine})_3]^{2+}$. *Chem. - A Eur. J.* **2013**, *19* (51), 17541–17551.

(7) van Veenendaal, M.; Chang, J.; Fedro, A. J. Model of Ultrafast Intersystem Crossing in Photoexcited Transition-Metal Organic Compounds. *Phys. Rev. Lett.* **2010**, *104* (6), 067401.

(8) Zhang, W.; Alonso-Mori, R.; Bergmann, U.; Bressler, C.; Chollet, M.; Galler, A.; Gawelda, W.; Hadt, R. G.; Hartsock, R. W.; Kroll, T.; Kjær, K. S.; Kubiček, K.; Lemke, H. T.; Liang, H. W.; Meyer, D. A.; Nielsen, M. M.; Purser, C.; Robinson, J. S.; Solomon, E. I.; Sun, Z.; Sokaras, D.; van Driel, T. B.; Vankó, G.; Weng, T.-C.; Zhu, D.; Gaffney, K. J. Tracking Excited-State Charge and Spin Dynamics in Iron Coordination Complexes. *Nature* **2014**, *509* (7500), 345–348.

(9) Auböck, G.; Chergui, M. Sub-50-Fs Photoinduced Spin Crossover in $[Fe(Bpy)_3]^{2+}$. *Nat. Chem.* **2015**, *7* (8), 629–633.

(10) Lemke, H. T.; Kjær, K. S.; Hartsock, R.; Van Driel, T. B.; Chollet, M.; Glownia, J. M.; Song, S.; Zhu, D.; Pace, E.; Matar, S. F.; Nielsen, M. M.; Benfatto, M.; Gaffney, K. J.; Collet, E.; Cammarata, M. Coherent Structural Trapping through Wave Packet Dispersion during Photoinduced Spin State Switching. *Nat. Commun.* **2017**, *8*, 15342.

(11) Ryland, E. S.; Lin, M.-F.; Verkamp, M. A.; Zhang, K.; Benke, K.; Carlson, M.; Vura-Weis, J. Tabletop Femtosecond M-Edge X-Ray Absorption Near-Edge Structure of FeTPPCl: Metalloporphyrin Photophysics from the Perspective of the Metal. *J. Am. Chem. Soc.* **2018**, *140* (13), 4691–4696.

(12) Chatterley, A. S.; Lackner, F.; Pemmaraju, C. D.; Neumark, D. M.; Leone, S. R.; Gessner, O. Dissociation Dynamics and Electronic Structures of Highly Excited Ferrocenium Ions Studied by Femtosecond XUV Absorption Spectroscopy. *J. Phys. Chem. A* **2016**, *120* (48), 9509–9518.

(13) Vura-Weis, J.; Jiang, C.-M.; Liu, C.; Gao, H.; Lucas, J. M.; de Groot, F. M. F.; Yang, P.; Alivisatos, A. P.; Leone, S. R. Femtosecond $M_{2,3}$-Edge Spectroscopy of Transition-Metal Oxides: Photoinduced Oxidation State Change in $\alpha\text{-}Fe_2O_3$. *J. Phys. Chem. Lett.* **2013**, *4* (21), 3667–3671.

(14) Zhang, K.; Girolami, G. S.; Vura-Weis, J. Improved Charge Transfer Multiplet Method to Simulate M - and L -Edge X-Ray Absorption Spectra of Metal-Centered Excited States. *J. Synchrotron Radiat.* **2018**, *25* (5), 1600–1608.

(15) Baker, L. R.; Jiang, C.-M.; Kelly, S. T.; Lucas, J. M.; Vura-Weis, J.; Gilles, M. K.; Alivisatos, A. P.; Leone, S. R. Charge Carrier Dynamics of Photoexcited Co_3O_4 in Methanol: Extending High Harmonic Transient Absorption Spectroscopy to Liquid Environments. *Nano Lett.* **2014**, *14* (10), 5883–5890.

(16) Zhang, K.; Lin, M. F.; Ryland, E. S.; Verkamp, M. a.; Benke, K.; De Groot, F. M. F.; Girolami, G. S.; Vura-Weis, J. Shrinking the Synchrotron: Tabletop Extreme Ultraviolet Absorption of Transition-Metal Complexes. *J. Phys. Chem. Lett.* **2016**, *7*, 3383–3387.

(17) Carneiro, L. M.; Cushing, S. K.; Liu, C.; Su, Y.; Yang, P.; Alivisatos, A. P.; Leone, S. R. Excitation-Wavelength-Dependent Small Polaron Trapping of Photoexcited Carriers in $\alpha\text{-}Fe_2O_3$. *Nat. Mater.* **2017**, *16* (8), 819–825.

(18) Cowan, R. . *Theory of Atomic Structure and Spectra*; University of California Press: Berkeley, CA, 1981.

(19) de Groot, F.; Kotani, A. *Core Level Spectroscopy of Solids*; CRC Press, 2008.

(20) Warner, B.; Oberg, J. C.; Gill, T. G.; El Hallak, F.; Hirjibehedin, C. F.; Serri, M.; Heutz, S.; Arrio, M.-A.; Sainctavit, P.; Mannini, M.; Poneti, G.; Sessoli, R.; Rosa, P. Temperature- and Light-Induced Spin Crossover Observed by X-Ray Spectroscopy on Isolated Fe(II) Complexes on Gold. *J. Phys. Chem. Lett.* **2013**, *4* (9), 1546–1552.

(21) Huse, N.; Cho, H.; Hong, K.; Jamula, L.; de Groot, F. M. F.; Kim, T. K.; McCusker, J. K.; Schoenlein, R. W. Femtosecond Soft X-Ray Spectroscopy of Solvated Transition-Metal Complexes: Deciphering the Interplay of Electronic and Structural Dynamics. *J. Phys. Chem. Lett.* **2011**, *2* (8), 880–884.

(22) Gawelda, W.; Cannizzo, A.; Pham, V. T.; Van Mourik, F.; Bressler, C.; Chergui, M. Ultrafast Nonadiabatic Dynamics of $[Fe^{II}(Bpy)_3]^{2+}$in Solution. *J. Am. Chem. Soc.* **2007**, *129* (26), 8199–8206.

(23) Nitzan, A. *Chemical Dynamics in Condensed Phases*; Oxford University Press: New York, 2006.

(24) Consani, C.; Prémont-Schwarz, M.; Elnahhas, A.; Bressler, C.; Van Mourik, F.; Cannizzo, A.; Chergui, M.

Vibrational Coherences and Relaxation in the High-Spin State of Aqueous $[Fe^{II}(Bpy)_3]^{2+}$. *Angew. Chemie - Int. Ed.* **2009**, *48* (39), 7184–7187.

(25) Monat, J. E.; McCusker, J. K. Femtosecond Excited-State Dynamics of an Iron(II) Polypyridyl Solar Cell Sensitizer Model. *J. Am. Chem. Soc.* **2000**, *122* (17), 4092–4097.

(26) Ronayne, K. L.; Paulsen, H.; Höfer, A.; Dennis, A. C.; Wolny, J. A.; Chumakov, A. I.; Schünemann, V.; Winkler, H.; Spiering, H.; Bousseksou, A.; Gütlich, P.; Trautwein, A. X.; McGarvey, J. J. Vibrational Spectrum of the Spin Crossover Complex $[Fe(Phen)_2(NCS)_2]$ Studied by IR and Raman Spectroscopy, Nuclear Inelastic Scattering and DFT Calculations. *Phys. Chem. Chem. Phys.* **2006**, *8* (40), 4685–4693.

(27) Cammarata, M.; Bertoni, R.; Lorenc, M.; Cailleau, H.; Di Matteo, S.; Mauriac, C.; Matar, S. F.; Lemke, H.; Chollet, M.; Ravy, S.; Laulhé, C.; Létard, J.-F.; Collet, E. Sequential Activation of Molecular Breathing and Bending during Spin-Crossover Photoswitching Revealed by Femtosecond Optical and X-Ray Absorption Spectroscopy. *Phys. Rev. Lett.* **2014**, *113* (22), 227402.

(28) Miller, N. A.; Deb, A.; Alonso-Mori, R.; Glownia, J. M.; Kiefer, L. M.; Konar, A.; Michocki, L. B.; Sikorski, M.; Sofferman, D. L.; Song, S.; Toda, M. J.; Wiley, T. E.; Zhu, D.; Kozlowski, P. M.; Kubarych, K. J.; Penner-Hahn, J. E.; Sension, R. J. Ultrafast X-Ray Absorption Near Edge Structure Reveals Ballistic Excited State Structural Dynamics. *J. Phys. Chem. A* **2018**, *122* (22), 4963–4971.

(29) Chábera, P.; Fredin, L. A.; Kjær, K. S.; Rosemann, N. W.; Lindh, L.; Prakash, O.; Liu, Y.; Wärnmark, K.; Uhlig, J.; Sundström, V.; Yartsev, A.; Persson, P. Band-Selective Dynamics in Charge-Transfer Excited Iron Carbene Complexes. *Faraday Discuss.* **2019**, DOI: 10.1039/c8fd00232k.

(30) Kjær, K. S.; Kaul, N.; Prakash, O.; Chábera, P.; Rosemann, N. W.; Honarfar, A.; Gordivska, O.; Fredin, L. A.; Bergquist, K.-E.; Häggström, L.; Ericsson, T.; Lindh, L.; Yartsev, A.; Styring, S.; Huang, P.; Uhlig, J.; Bendix, J.; Strand, D.; Sundström, V.; Persson, P.; Lomoth, R.; Wärnmark, K. Luminescence and Reactivity of a Charge-Transfer Excited Iron Complex with Nanosecond Lifetime. *Science* **2019**, *363* (6424), 249–253.

(31) Damrauer, N. H.; Cerullo, G.; Yeh, A.; Boussie, T. R.; Shank, C. V.; McCusker, J. K. Femtosecond Dynamics of Excited-State Evolution in $[Ru(Bpy)_3]^{2+}$. *Science* **1997**, *275* (5296), 54–57.

(32) Lee, N.; Petrenko, T.; Bergmann, U.; Neese, F.; DeBeer, S. Probing Valence Orbital Composition with Iron Kβ X-Ray Emission Spectroscopy. *J. Am. Chem. Soc.* **2010**, *132* (28), 9715–9727.

(33) Peng, G.; deGroot, F. M. F.; Haemaelaeinen, K.; Moore, J. A.; Wang, X.; Grush, M. M.; Hastings, J. B.; Siddons, D. P.; Armstrong, W. H. High-Resolution Manganese x-Ray Fluorescence Spectroscopy. Oxidation-State and Spin-State Sensitivity. *J. Am. Chem. Soc.* **1994**, *116* (7), 2914–2920.

(34) Huse, N.; Kim, T. K.; Jamula, L.; McCusker, J. K.; De Groot, F. M. F.; Schoenlein, R. W. Photo-Induced Spin-State Conversion in Solvated Transition Metal Complexes Probed via Time-Resolved Soft X-Ray Spectroscopy. *J. Am. Chem. Soc.* **2010**, *132* (19), 6809–6816.

(35) Kjær, K. S.; Kunnus, K.; Harlang, T. C. B.; Van Driel, T. B.; Ledbetter, K.; Hartsock, R. W.; Reinhard, M. E.; Koroidov, S.; Li, L.; Laursen, M. G.; Biasin, E.; Hansen, F. B.; Vester, P.; Christensen, M.; Haldrup, K.; Nielsen, M. M.; Chabera, P.; Liu, Y.; Tatsuno, H.; Timm, C.; Uhlig, J.; Sundstöm, V.; Németh, Z.; Szemes, D. S.; Bajnóczi, É.; Vankó, G.; Alonso-Mori, R.; Glownia, J. M.; Nelson, S.; Sikorski, M.; Sokaras, D.; Lemke, H. T.; Canton, S. E.; Wärnmark, K.; Persson, P.; Cordones, A. A.; Gaffney, K. J. Solvent Control of Charge Transfer Excited State Relaxation Pathways in $[Fe(2,2'\text{-Bipyridine})(CN)_4]^{2-}$. *Phys. Chem. Chem. Phys.* **2018**, *20* (6), 4238–4249.

(36) Koralek, J. D.; Kim, J. B.; Brůža, P.; Curry, C. B.; Chen, Z.; Bechtel, H. A.; Cordones, A. A.; Sperling, P.; Toleikis, S.; Kern, J. F.; Moeller, S. P.; Glenzer, S. H.; DePonte, D. P. Generation and Characterization of Ultrathin Free-Flowing Liquid Sheets. *Nat. Commun.* **2018**, *9* (1), 1353.

(37) Ekimova, M.; Quevedo, W.; Faubel, M.; Wernet, P.; Nibbering, E. T. J. A Liquid Flatjet System for Solution Phase Soft-x-Ray Spectroscopy. *Struct. Dyn.* **2015**, *2* (5), 054301.

Supporting Information for

Tracking the Metal-Centered Triplet in Photoinduced Spin Crossover of $Fe(phen)_3^{2+}$ with Tabletop Femtosecond Transient M-edge XANES

Kaili Zhang, Ryan Ash, Gregory S. Girolami, Josh Vura-Weis

Table of Contents

S1 Additional data collection and experimental details

The instrument layout is shown in Figure S1A. A typical spectrum of the probe beam is shown in Figure S1B. At the sample position, the probe beam size was measured using a knife-edge scan to be 80 µm FWHM and the pump beam set to be ~200 µm FWHM. The sample was pumped at 3.5 mJ/cm^2, corresponding to ~12% excitation per pulse. This excitation fraction is calculated using the known pump fluence and the sample absorbance at 535 nm. Nitrogen gas cooling was employed to avoid sample heating and damage.[1] Neither pump-induced nor XUV-induced damage was observed under these conditions, confirmed by periodically comparing ground state absorption of a pumped area on the sample to a pristine area. During processing, ~10% of scans were discarded due to fluctuations in the XUV probe. The spectral region from 65-67 eV was averaged and any single scan which differed from the average by ± 4 mA was discarded. This data set was collected over three days for a total of ~30 hours of data collection including concurrent α-Fe_2O_3 transient absorption.

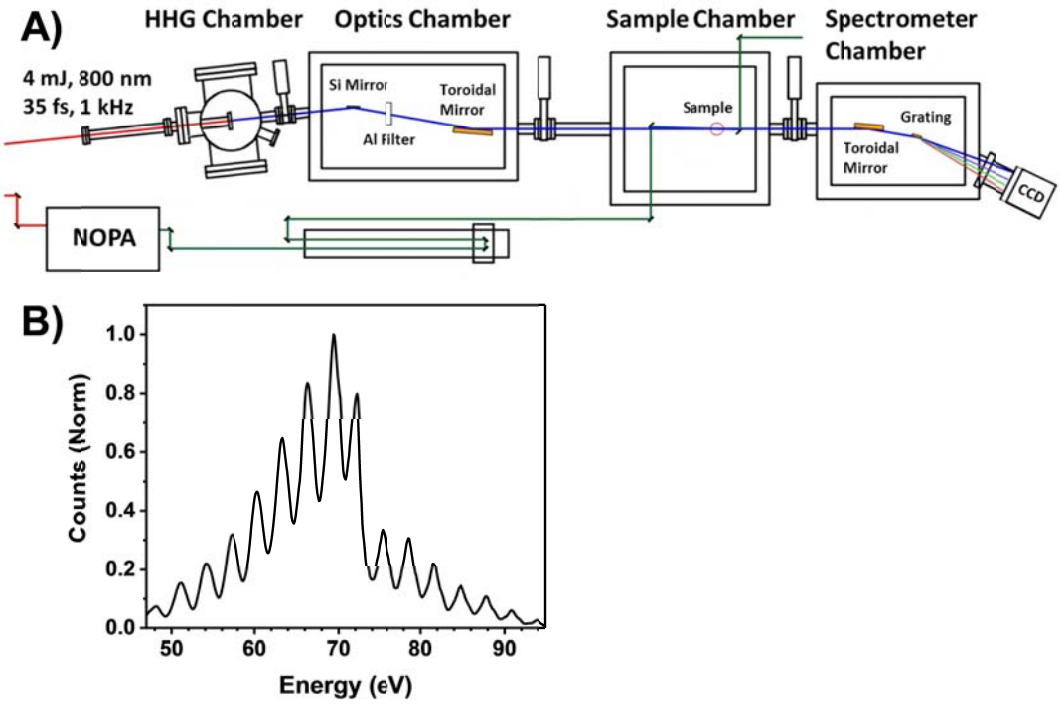

Figure S1 A) Instrument layout B) Typical spectrum of probe beam. Odd harmonics of the 800 nm driving laser field appear as peaks every 3.1 eV, but the broad continuum beneath them is suitable for absorption spectroscopy. The step at 72 eV is caused by absorption by the Al filter used to attenuate residual 800 nm photons

True time zero drifts by ~40 fs over the course of the experiment due to room temperature fluctuations. We accounted for this drift by measuring the IRF-limited rise of the LMCT signal in α-Fe_2O_3 every 3-4 hours. Transient absorption spectroscopy of $Fe(phen)_3$ is collected in 40-minute increments, and the time axis for each such run is corrected by interpolating between the α-Fe_2O_3 references. A kinetic trace of α-Fe_2O_3 used to determine t_0 and the width of the IRF is shown in Figure S2A, with a representative day of data collection shown in Figure S2B. The full $Fe(phen)_3$ data set is then binned in 10 fs intervals for the first 300 fs and in 25 fs intervals thereafter. To account for changes in pump fluence over multiple days of data collection, each data run was scaled by a factor to set the average of the main high-spin peak (56.5-57.5 eV) between 500-1000 fs to 13 mA.

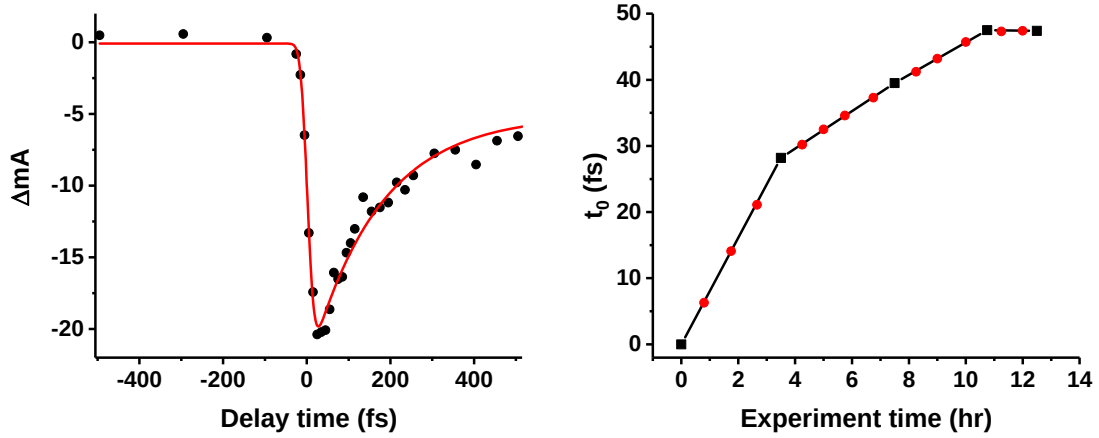

Figure S2: A) Fit (red) of the bleach seen in the transient data (black) of α-Fe_2O_3 pumping at 535 nm. This fit was used to extract t_0 for $Fe(phen)_3^{2+}$ runs. B) Determination of t_0 for $Fe(phen)_3^{2+}$ runs (red circles) by linearly interpolating between α-Fe_2O_3 runs throughout the day (black squares).

S2 Thermal Spin-Crossover of $Fe(H_2B(pz)_2)_2bpy$

$Fe(H_2B(pz)_2)_2bpy$ was synthesized according to published procedures.[2] The sample consisted of a ~150 nm thick film deposited on a 100 nm Si_3N_4 free-standing membrane by vacuum sublimation. To collect variable temperature $M_{2,3}$-edge spectra, a thin film of $Fe(H_2B(pz)_2)_2bpy$ was loaded into a home-built bath cryostat, with a temperature range of 85 – 300 K. An aluminum sample cell is attached to a liquid nitrogen filled cold finger via a small copper rod, with an aluminum flange making up the base of the cold finger to increase heat transfer to the sample cell. The cold finger is attached to a 3-axis manipulator out of vacuum which moves the sample into the XUV beam path. Spectra were collected at 295 (HS) and 85 (LS) K using the same sample on the same day.

S3 Sample preparation of $Fe(phen)_3(SCN)_2$

Thin films of $Fe(phen)_3(SCN)_2$ were prepared by reactive sublimation of $Fe(phen)_2(NCS)_2$ as described by Ellingsworth et al.[3] $Fe(phen)_2(NCS)_2$ powder was loaded into a boron nitride crucible and loaded into a homebuilt vacuum sublimation chamber. The chamber was pumped down to a pressure of ~$1x10^{-5}$ Torr and the crucible heated to 300 °C. UV-Vis spectra of the films were then recorded to confirm the complex was deposited as $Fe(phen)_3(SCN)_2$ and to estimate sample thickness (Figure S3).

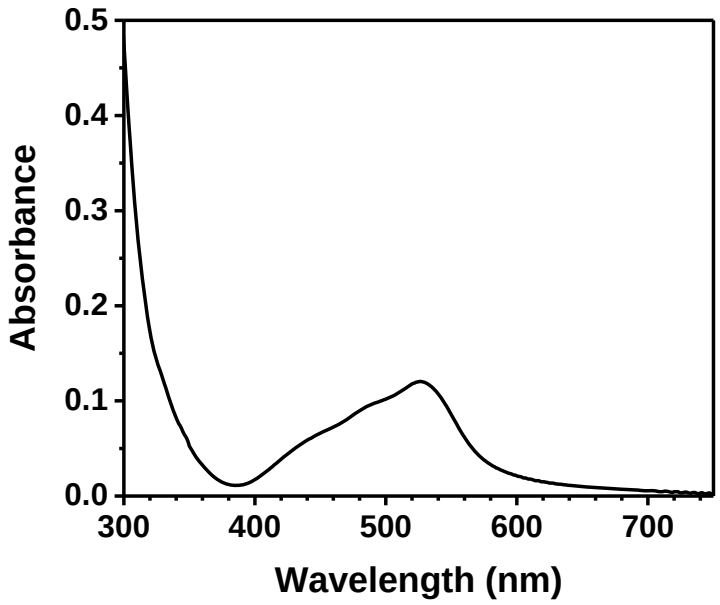

Figure S3 UV/Vis spectrum of a film of $Fe(phen)_3(SCN)_2$ as deposited

S4 Spin boson model of visible-pump XUV-probe response

The spin-boson model used here (and the nomenclature below) is adapted from Nitzan.[4] Let us first consider the general case of the linear absorption spectrum from a coherent state that consists of a manifold of N closely spaced nondegenerate eigenfunctions (denoted $|n\rangle$ with eigenvalues E_n) and energetically separated upper states (denoted $|c\rangle$ with eigenvalues E_c such that $E_c \gg E_n$ for any n or c). In this basis, the Hamiltonian is given by $\widehat{H} = \sum_n E_n|n\rangle\langle n| + \sum_c E_c|c\rangle\langle c|$ and the density matrix describing this coherent state is $\hat{\rho} = \sum_{m,n=1}^{N} \rho_{mn}|m\rangle\langle n|$. The density matrix is assumed to evolve slowly so that it is assumed to be constant on the time scale of $n \rightarrow c$ transitions.

In the relevant spectral region the transition dipole moment operator is given by $\hat{\mu} = \sum_{n,c} \mu_{nc}(|n\rangle\langle c| + |n\rangle\langle c|)$. Let $\hat{\mu}(t) = e^{i\frac{H}{\hbar}t}\hat{\mu}e^{-i\frac{H}{\hbar}t}$.

The linear absorbance is then given by $\alpha(\Omega) = Im\left[\int_0^\infty \chi(t)e^{i\Omega t}dt\right]$ where $\chi(t) = \frac{i}{\hbar}Tr\{[\hat{\mu}(t), \hat{\mu}]\hat{\rho}\}$ is the dipole correlation function and Ω is the angular frequency.

It can be shown that $\chi(t) = \frac{i}{\hbar}Tr\{[\hat{\mu}(t), \hat{\mu}]\hat{\rho}\} = \frac{2}{\hbar}\sum_{n,c} \sin\left(\frac{E_{cn}}{\hbar}t\right)\mu_{nc}^2\rho_{nn} - \frac{2}{\hbar}\sum_{m>n,c}\left(Im\left(\rho_{nm}e^{i\frac{E_{nc}}{\hbar}t}\right) + Im\left(\rho_{mn}e^{i\frac{E_{mc}}{\hbar}t}\right)\right)\mu_{nc}\mu_{mc}$ where $E_{ab} = E_a - E_b$.

Therefore, $\alpha(\Omega) = \frac{2}{\hbar}\sum_{n,c}\mu_{nc}^2\rho_{nn}L\left(\Omega - \frac{E_{cn}}{\hbar}\right) + \frac{2}{\hbar}\sum_{m>n,c}\mu_{nc}\mu_{mc}\left\{Re(\rho_{nm})\left[L\left(\Omega - \frac{E_{cn}}{\hbar}\right) + L\left(\Omega - \frac{E_{cm}}{\hbar}\right)\right] - Im(\rho_{nm})\left[L'\left(\Omega - \frac{E_{cn}}{\hbar}\right) - L'\left(\Omega - \frac{E_{cm}}{\hbar}\right)\right]\right\}$, where $L(\Omega) = \frac{\Gamma/2}{\Omega^2+\Gamma^2}$ and $L'(\omega) = \frac{\Omega/2}{\Omega^2+\Gamma^2}$ and Γ

is the intrinsic linewidth of $n \to c$ transitions. Note here that emissive components such as $L\left(\omega + \frac{E_{cn}}{\hbar}\right)$ have been omitted. If the interlevel spacing between $|n\rangle$ is small compared to Γ, then $\left|L'\left(\Omega - \frac{E_{cn}}{\hbar}\right) - L'\left(\Omega - \frac{E_{cm}}{\hbar}\right)\right| \leq \frac{|E_m - E_n|}{\hbar\Gamma^2} \approx 0$. This approximation holds for the M-edge transitions in this work, where $|n\rangle$ are eigenfunctions of a ligand cage breathing mode of about 100-200 cm^{-1} and Γ =10^3-10^4 cm^{-1} for the linewidth of each XUV absorption peak.

Therefore, the absorption spectrum is given by

$\alpha(\Omega) = \frac{2}{\hbar}\sum_{n,c}\mu_{nc}^2\rho_{nn}L\left(\Omega - \frac{E_{cn}}{\hbar}\right) + \frac{4}{\hbar}\sum_{m>n,c}\mu_{nc}\mu_{mc}Re(\rho_{nm})L\left(\Omega - \frac{E_{cn}}{\hbar}\right)$ or

$\alpha(\mathrm{E}) = \frac{2}{\hbar}\sum_{n,c}\mu_{nc}^2\rho_{nn}L(\mathrm{E} - E_{cn}) + \frac{4}{\hbar}\sum_{m>n,c}\mu_{nc}\mu_{mc}Re(\rho_{nm})L(\mathrm{E} - E_{cn})$ in terms of energy.

Let us now consider the case of pump-probe response of vibronic spin-crossover system. We denote the MLCT state as State 0, the intermediate as State 1, and the $^5T_{2g}$ state as State 2. We only consider the vibronic levels of State 2, denoted as States 2n for n=0,1,…. We assume that the density matrix is of the following form $\rho_{mn} = \begin{pmatrix} \rho_{0,0} & 0 & 0 & 0 & \cdots \\ 0 & \rho_{1,1} & 0 & 0 & \cdots \\ 0 & 0 & \rho_{20,20} & \rho_{20,21} & \cdots \\ 0 & 0 & \rho_{21,20} & \rho_{21,21} & \cdots \\ \vdots & \vdots & \vdots & \vdots & \ddots \end{pmatrix}$. More specifically, we assume that there is no coherence between States 0 and 1, between State 0 and any of States 2n or between State 1 and any of States 2n.

The time evolution of $\hat{\rho}$ is given by the phenomenological master equation as follows:

$$\frac{d\rho_{0,0}}{dt} = -\frac{1}{\tau_1}\rho_{0,0} + IRF(t;\sigma)$$

$$\frac{d\rho_{1,1}}{dt} = -\frac{1}{\tau_2}\rho_{1,1} + \frac{1}{\tau_1}\rho_{0,0}$$

$$\frac{d\rho_{2m,2n}}{dt} = \left(i(m-n)\omega - \frac{1}{\tau_d}\right)(1-\delta_{mn})\rho_{2m,2n} + \frac{A_{mn}}{\tau_2}\rho_{1,1}$$

where $\mathrm{IRF}(t;\sigma) = \frac{1}{\sigma\sqrt{2\pi}}e^{-t^2/2\sigma^2}$ is the instrument response function, $\omega = \frac{2\pi}{T}$ is the fundamental angular frequency of the vibrational levels, T is the fundamental oscillation period, τ_d the damping time and $\hat{A} = \sum_{m,n}A_{mn}|2m\rangle\langle 2n| = \sum_{m,n}\langle 2m|1\rangle\langle 1|2n\rangle|2m\rangle\langle 2n|$ is the projection of the intermediate state onto the vibronic states $|2n\rangle$.

To simplify the explicit expressions of the density matrix elements and the overall difference spectrum, we define the following functions:

$$u_g(t;\sigma) = u(t) * \mathrm{IRF}(t;\sigma) = \frac{1}{2}\left(1 + \mathrm{erf}\left(\frac{t}{\sigma\sqrt{2}}\right)\right)$$

$$\exp_g(t;\tau,\sigma) = \left[u(t)e^{-t/\tau}\right] * \mathrm{IRF}(t;\sigma) = \frac{1}{2}e^{-\frac{t\tau-\sigma^2}{2\tau^2}}\left[1+\mathrm{erf}\left(\frac{t\tau-\sigma^2}{\tau\sigma\sqrt{2}}\right)\right]$$

$$\cos_g(t;T,\tau,\phi,\sigma) = \left[u(t)e^{-t/\tau}\cos\left(\frac{2\pi}{T}t+\phi\right)\right] * \mathrm{IRF}(t;\sigma)$$
$$= \frac{e^{-2\pi^2\sigma^2/T^2 - t/\tau}}{2}\mathrm{Re}\left[e^{i\left(\frac{2\pi}{T}t+\phi\right)}\left(1+\mathrm{erf}\left(\frac{t\tau T-(2\pi\tau i-T)\sigma^2}{T\tau\sigma\sqrt{2}}\right)\right)\right]$$

where $u(t)$ is the step function and $\mathrm{erf}(t)$ is the error function.

Using these expressions, the solutions to the first two equations can be expressed as $\rho_{0,0}(t) = \exp_g(t,\tau_1;\sigma)$ and $\rho_{1,1}(t) = \frac{\tau_2}{\tau_2-\tau_1}\left[\exp_g(t,\tau_2;\sigma) - \exp_g(t,\tau_1;\sigma)\right]$. The corresponding contributions to the difference spectrum are $\alpha_0(\mathrm{E},t) = S_0(\mathrm{E})\rho_{0,0}(t)$ and $\alpha_1(\mathrm{E},t) = S_1(\mathrm{E})\rho_{1,1}(t)$, where $S_0(E) = \frac{2}{\hbar}\sum_c \mu_{0c}^2 L(\mathrm{E}-E_{c0})$ and $S_1(\Omega) = \frac{2}{\hbar}\sum_c \mu_{1c}^2 L(\mathrm{E}-E_{c1})$ are difference spectra of the MLCT state and State 1. $S_0(\Omega)$ and $S_1(\Omega)$ are treated as vectors of free parameters.

Solving the third equation gives that $\rho_{2n,2n}(t) = A_{nn}u(t) * \rho_{1,1}(t)/\tau_2$ for the diagonal elements and $\rho_{2m,2n}(t) = A_{mn}\left[e^{i(m-n)\omega t}u(t)\right] * \rho_{1,1}(t)/\tau_2$ for the coherences where $u(t)$ is the step function.

The contribution to absorption spectrum from the $^5T_{2g}$ state is then

$\alpha_2(\mathrm{E},t) =$
$\frac{2}{\hbar}\sum_{n,c}\mu_{nc}^2 A_{nn}u(t) * \rho_{1,1}(t)L\left(\mathrm{E}-E_{c,2n}\right)/\tau_2 + \frac{4}{\hbar}\sum_{m>n}\mu_{nc}\mu_{mc}Re\left(A_{mn}\left[e^{i(m-n)\omega t - t/\tau_d}u(t)\right] * \rho_{1,1}(t)/\tau_2\right)L\left(\mathrm{E}-E_{c,2n}\right)$.

If only coherences between neighboring levels are included, then

$\alpha_2(\mathrm{E},t) = \frac{2}{\hbar}\sum_{n,c}\mu_{nc}^2 A_{nn}u(t) * \rho_{1,1}(t)L\left(\mathrm{E}-E_{c,2n}\right)/\tau_2 + \frac{4}{\hbar}\sum_{n,c}\mu_{nc}\mu_{n+1,c}Re\left(A_{n+1,n}\left[e^{i\omega t - t/\tau_d}u(t)\right] * \rho_{1,1}(t)/\tau_2\right)L\left(\mathrm{E}-E_{c,2n}\right)$.

Separating the time-dependent and energy-dependent parts gives, $\alpha_2(\mathrm{E},t) = S_2(\mathrm{E})\rho_{22}(t) + S_2'(\mathrm{E})\rho'(t)$. The time-dependent factors are
$\rho_{2,2}(t) = u_g(t;\sigma) - \frac{\tau_2}{\tau_2-\tau_1}\exp_g(t,\tau_1;\sigma) + \frac{\tau_1}{\tau_2-\tau_1}\exp_g(t,\tau_2;\sigma)$, $\rho'(t) = \frac{1}{\tau_2-\tau_1}\left[\exp_g(t,\tau_2;\sigma)\frac{\cos\phi_2}{R_2} - \exp_g(t,\tau_1;\sigma)\frac{\cos\phi_1}{R_1}\right] + \frac{1}{\tau_1\tau_2}\cos_g(t;T,\tau_d,\phi_1+\phi_2,\sigma)$ where $R_x = \sqrt{\left(1/\tau_d - 1/\tau_x\right)^2 + \left(\frac{2\pi}{T}\right)^2}$ and $\phi_x = \mathrm{Arg}\left(\frac{2\pi}{T} + i\left(1/\tau_d - 1/\tau_x\right)\right)$ for $x = 1,2$. The energy-dependent factors are
$S_2(\mathrm{E}) = \frac{2}{\hbar}\sum_{n,c}\mu_{nc}^2 A_{nn}L\left(\mathrm{E}-E_{c,2n}\right)$ and $S_3(\mathrm{E}) = \frac{4}{\hbar}\sum_{n,c}\mu_{nc}\mu_{n+1,c}L\left(\mathrm{E}-E_{c,2n}\right)$, corresponding to the

difference spectrum of the $^5T_{2g}$ state and the energy-dependent oscillation amplitude which is equal to twice the difference between the Frank-Condon spectrum and the averaged spectrum of $^5T_{2g}$.

In summary, the model of visible-pump-XUV-probe responses is given by $S(E,t) = S_0(\mathrm{E})\rho_{0,0}(t) + S_1(\mathrm{E})\rho_{1,1}(t) + S_2(\mathrm{E})\rho_{2,2}(t) + S_3(\mathrm{E})\rho'(t)$, having four scalar parameters τ_1, τ_2, T and τ_d and four vectorial parameters $S_0(\mathrm{E})$, $S_1(\mathrm{E})$, $S_2(\mathrm{E})$, $S_3(\mathrm{E})$.

S5 Exploration of fitting parameter space by random sampling

In order to assess the extent to which our choice of starting parameters is biasing the result of the fit, we conducted a broad exploration of the parameter space by initiating least squares refinement from randomly generated starting conditions. Least squares refinement was carried out using a method based on the variable projection method of Golub and Pereya[5]. Here, we will give a brief description of the method.

Let Y be a matrix containing the pump-probe signals with each row being a difference spectrum at the corresponding delay time. Let W be a matrix containing inverses of the standard errors of pump-probe observations. Let $A(\vec{\alpha})$ be a matrix containing the time-dependent part of the model i.e. a row j of $A(\vec{\alpha})$ is $\begin{bmatrix}\rho_{0,0}(t_j) & \rho_{1,1}(t_j) & \rho_{2,2}(t_j) & \rho'(t_j)\end{bmatrix}$. The kinetic parameters of the model are absorbed into the vector argument i.e. $\vec{\alpha} = [\tau_1 \quad \tau_2 \quad T \quad \tau_d]$. The spectral parameters are absorbed into the matrix $S = [S_0(\mathrm{E}) \quad S_1(\mathrm{E}) \quad S_2(\mathrm{E}) \quad S_3(\mathrm{E})]$ where the rows range over the energy points.

The goal is then to find the optimal $\vec{\alpha}$ and S that minimize $\|(Y - A(\vec{\alpha})S^T) \circ W\|_F^2$ where $\|\cdot\|_F^2$ denotes Frobenius 2-norm and $\circ$ denotes element-wise product. It can be shown that given a fixed $\vec{\alpha}$, the corresponding optimal is given by $S^*(\vec{\alpha}) = \begin{bmatrix}\vec{s}_1^*(\vec{\alpha}) & \vec{s}_2^*(\vec{\alpha}) & \cdots & \vec{s}_j^*(\vec{\alpha}) & \cdots\end{bmatrix}^T$ where $\vec{s}_j^*(\vec{\alpha}) = A^{(j)+}(y_j \circ w_j)$, $A^{(j)} = \mathrm{diag}(w_j)A(\vec{\alpha})$, y_j (and w_j) are the j'th column of Y (and W), and $(\cdot)^+$ denotes the Moore-Penrose inverse. Therefore, the problem is reduced to finding the optimal $\vec{\alpha}$ that minimizes $\|(Y - A(\vec{\alpha})S^*(\vec{\alpha})^T) \circ W\|_F^2$.

This algorithm was implemented using the SciPy (version 1.2.1) package running on Python 2.7.15. Randomized starting parameters were drawn from uniform distributions (Table S1).

Table S1 Ranges of the uniform distributions of the kinetic parameters

	Range
τ_1 (fs)	10 – 300
τ_2 (fs)	10 – 300
T (fs)	201 – 299
τ_d (fs)	300 – 2000

One hundred trials were carried out. The outcomes fall into five classes (Table S2). The vast majority of trials converged to either of two classes of outcomes (classes 3 and 4) corresponding to inverted kinetics (τ_1>τ_2) and non-inverted kinetics, respectively. The fits from Class 3 are used in the main text, as the inverted kinetic description is standard in the literature of Fe^{II} spin crossover.

Table S2 Summary of random trial outcomes

Class	Average parameters	Average cost	Count
1	τ_1 =178 fs, τ_2 = 2 fs, T = 268 fs, τ_d = 411 fs	105863	1
2	τ_1 =88 fs, τ_2 = 88 fs, T = 417 fs, τ_d = 114 fs	103325	1
3	τ_1 =170 fs, τ_2 = 40 fs, T = 250 fs, τ_d = 657 fs	100847	50
4	τ_1 =40 fs, τ_2 = 170 fs, T = 250 fs, τ_d = 657 fs	100847	47
5	Failed to converge		1

The component spectra corresponding to the MLCT state, the $^5T_{2g}$ state and the oscillation amplitude attained in class 3 and class 4 outcomes are exactly superimposable. The component spectra corresponding to the ^3T state differ in magnitude but the shape is largely identical (Figure S4).

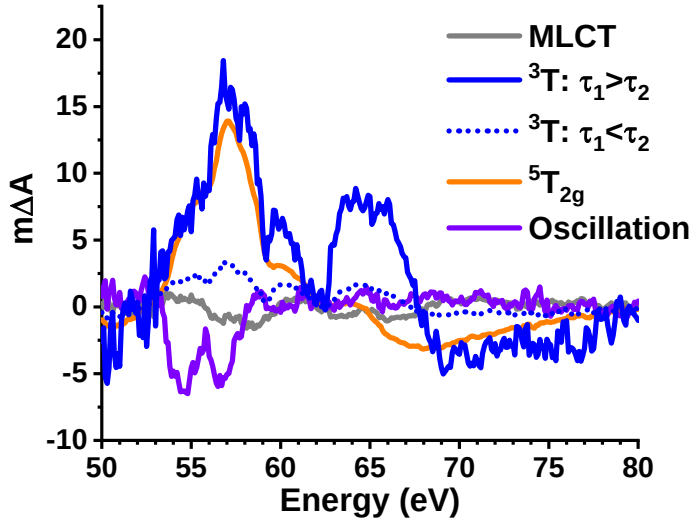

Figure S4 Component spectra attained in class 3 and class 4 outcomes

S6 Kinetic modeling results neglecting the triplet contribution

The component spectra extracted using a kinetic model analogous to that described in Section S4 but with triplet deleted are shown below (Figure S5 right). The component spectrum of the $^5T_{2g}$ state is nearly identical to that extracted from the full model, whereas those of the oscillation amplitude and the MLCT state differ slightly in the region around 65 eV.

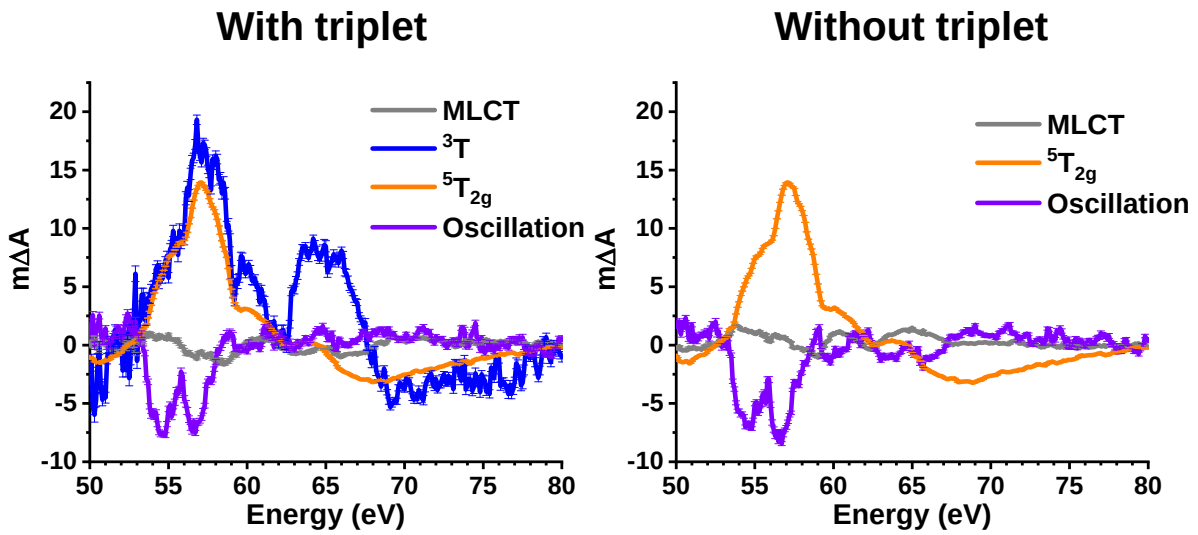

Figure S5 Component spectra extracted from kinetic models with or without triplet

The residual maps (reconstruction minus experiment) of the models and energy slices at select times are shown in Figure S6. It is clear that the model without the triplet is unable to fully account for the pump-probe signals around 65 eV, especially at around 10 fs and at around 100 fs (Figure S6D), even with the modifications in the MLCT spectrum and the oscillation amplitude. Including the triplet not only better accounts for the experimental signal around 65 eV at early times, but also leads to an overall reduction in residual (Figure S6A&B).

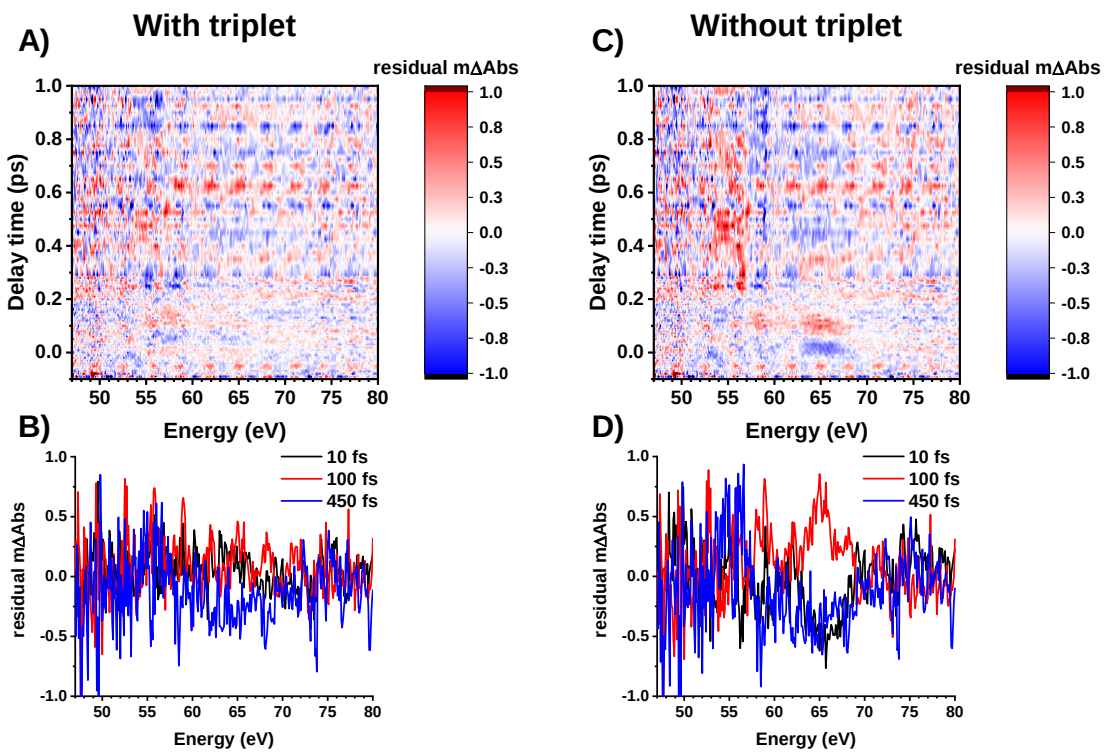

Figure S6 Residual maps and residual vs. energy plots at select delay times

S7 LFM simulation parameters and simulated spectra of $^3T_{1g}$ and $^3T_{2g}$ states

Table S3 LFM simulation parameters

	10Dq (eV)	Fdd scaling	Fpd & Gpd scaling	Horizontal shift (eV)	Intensity scale
MLCT	2.0	0.625	0.625	56.2	0.6
$^3T_{1g}$	2.2	1.0	0.8	55.2	1.0
$^3T_{2g}$	2.2	1.0	0.8	55.2	1.0
$^5T_{2g}$	0.6	1.0	0.8	55.2	1.0
$^1A_{1g}$	2.6	1.0	0.625	56.4	0.6

The parameters used for LFM simulation of difference spectra are in (Table S3). The simulated absorption spectra and difference spectra relative to $^1A_{1g}$ of $^3T_{1g}$ and $^3T_{2g}$ states are shown in Figure S7 and Figure S8. The only major difference between the two is the height and width of the peak around 57 eV.

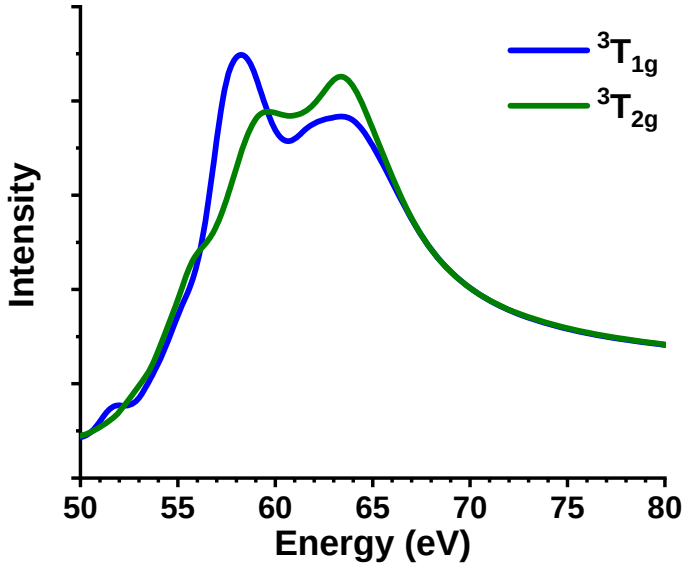

Figure S7 Simulated absorption spectra of $^3T_{1g}$ and $^3T_{2g}$ states

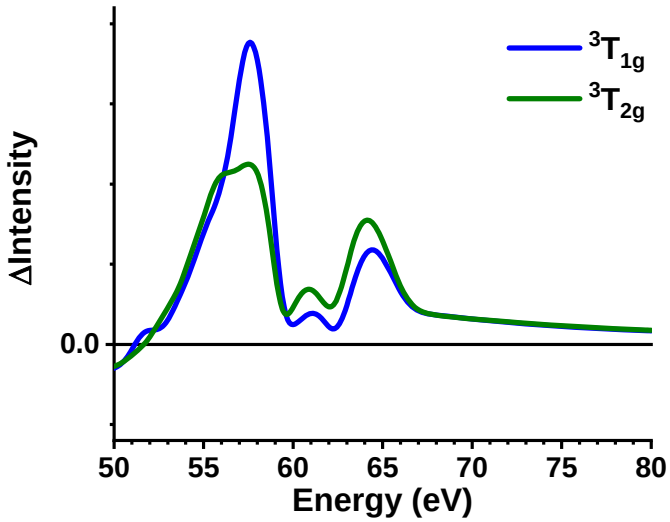

Figure S8 Simulated difference spectra of $^3T_{1g}$ and $^3T_{2g}$ states

LFM theory analysis shows that the $M_{2,3}$-edge spectra of $^3T_{1g}$ and $^3T_{2g}$ states contain three features: two transitions at around 55 eV and at 57 eV that become merged in $^3T_{1g}$ and a transition at around 65 eV. In the weak field limit, the lower energy features are transitions from the ^3H term of a free Fe^{2+} ion to a manifold of triplet core-hole excited states whereas the higher energy feature is a transition to a higher ^3G term. As the ligand field is increased, the ground and excited configuration states are remixed and

shift slightly in energy, but the overall three-feature structure is preserved (Figure S9). We note that as opposed to the M-edge transitions from the singlet and quintet states (Figure 1B in the main text), the transitions from the triplet states are difficult to describe intuitively, as spin-orbit coupling mixes the closely-spaced core-hole states. For example, whereas in the singlet, the lowest-energy transition on the weak-field side is a combination of ^{5}F and ^{5}D, the lowest-energy transition for the triplet is a combination of two ^{3}H, three ^{3}G, one ^{3}F, and one ^{3}I states.

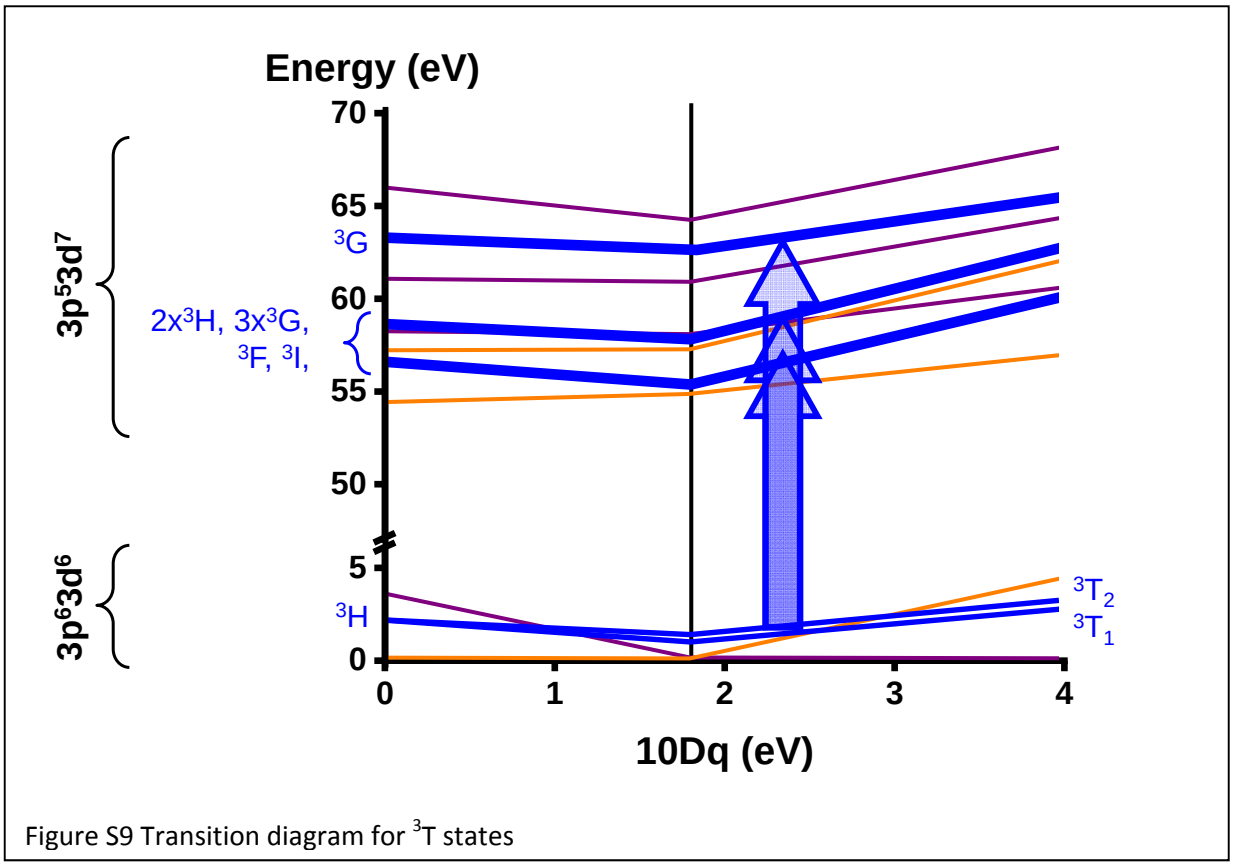

Figure S9 Transition diagram for ^{3}T states

S8 Weak amplitude of MLCT spectrum

The low intensity of the initial photoinduced ^{1,3}MLCT state is caused by a coincidental similarity between the ground state and excited-state spectra. As shown in Figure S10, LFM simulations predict that the $M_{2,3}$-edge spectrum of the MLCT state would have a three-peak structure similar to that of the $^1A_{1g}$ ground state. Furthermore, because of the increased spin and orbital angular momentum of the MLCT state (Fe^{III} $^2T_{2g}$) compared to the $^1A_{1g}$ state, the core-hole excited states of the MLCT state experience additional exchange stabilization compared to those of the $^1A_{1g}$ state. This effect tends to red-shift absorption features and counteracts the overall blue-shift that usually accompanies an increase in formal oxidation state. The consequent spectral overlap between the MLCT and $^1A_{1g}$ states leads to the MLCT state having a relatively subdued transient response. This spectrum is also consistent with an initial photoexcitation that is largely ligand-centered (with only partial MLCT character). As the initial MLCT state is widely accepted for Fe(II) polypyridyl complexes, we consider the ligand-centered explanation unlikely.

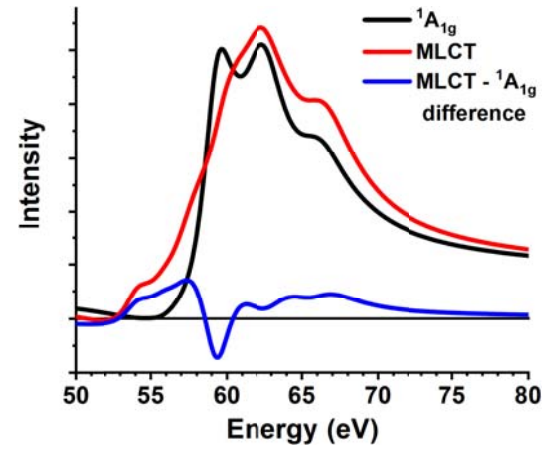

Figure S10: Simulated transient spectrum of the initial ^{1,3}MLCT state. The $^1A_{1g}$ ground state and the ^{1,3}MLCT state have similar spectra, so their difference is close to zero.

S9 Density functional theory calculations

DFT calculations were performed using Gaussian 09[6]. All structures were optimized under B3LYP functional in 6-31G* basis set with pure D basis functions (5D) and ultrafine integration grid.

The optimal atomic coordinates in Angstroms for the singlet and quintet states are listed below

	Singlet			Quintet		
Fe	-2.2E-05	-0.00087	0.000005	0.000917	0.00042	0.000583
N	1.693302	-0.09575	1.068821	1.253951	1.402061	1.145811
N	0.911751	-1.43252	-1.06661	1.904908	0.03216	-1.12269
N	0.786035	1.503648	-1.06638	-0.99131	1.595826	-1.14694
C	2.072654	0.610059	2.138118	0.913245	2.094211	2.233477

C	3.3195	0.438568	2.765106	1.773263	3.012946	2.858184
C	4.209988	-0.49755	2.27275	3.035136	3.210367	2.330753
C	3.847297	-1.26287	1.141555	3.430291	2.497108	1.175807
C	2.575256	-1.01561	0.57504	2.489992	1.600798	0.606371
C	4.68545	-2.26673	0.546603	4.725125	2.643472	0.573904
C	4.271016	-2.97559	-0.54394	5.064282	1.931888	-0.53794
C	2.14592	-1.74996	-0.57277	2.8414	0.862868	-0.5831
C	2.985112	-2.73759	-1.13892	4.132899	1.024625	-1.14635
C	2.495752	-3.42965	-2.26961	4.438372	0.272843	-2.30421
C	1.243044	-3.11306	-2.76175	3.486657	-0.57547	-2.83591
C	0.482351	-2.11007	-2.13525	2.230547	-0.66509	-2.21112
C	1.588982	1.469681	-2.1339	-0.53712	2.216304	-2.23637
C	2.079594	2.629384	-2.7596	-1.22615	3.268306	-2.86288
C	1.728216	3.872941	-2.2679	-2.43462	3.681677	-2.33543
C	0.882473	3.951674	-1.13858	-2.94604	3.049921	-1.17866
C	0.444419	2.731595	-0.57313	-2.17408	2.006079	-0.60744
C	0.445952	5.184818	-0.54447	-4.19569	3.418997	-0.5766
N	-1.69445	-0.07339	-1.06881	-0.88359	-1.64782	-1.14577
N	-0.93062	-1.42033	1.066637	0.583978	-1.7771	1.145988
N	-0.76612	1.513928	1.066352	-1.86755	0.363597	1.124999
C	-2.06445	0.637347	-2.13812	-1.6213	-1.5769	-2.25542
C	-3.31345	0.482311	-2.76511	-2.16015	-2.70553	-2.89483
C	-4.21621	-0.44198	-2.27276	-1.92075	-3.95628	-2.35821
C	-3.86365	-1.21201	-1.14155	-1.14695	-4.07266	-1.18162
C	-2.58846	-0.98154	-0.57503	-0.64926	-2.87687	-0.60224
C	-4.71497	-2.20472	-0.5466	-0.85	-5.33485	-0.56586
C	-4.30993	-2.91898	0.543953	-0.09532	-5.40134	0.566991
C	-2.16886	-1.72147	0.572787	0.137717	-2.9462	0.60285
C	-3.02101	-2.69795	1.13894	0.418389	-4.21058	1.182373
C	-2.54083	-3.39638	2.269647	1.201265	-4.23137	2.358538
C	-1.28406	-3.09632	2.761803	1.656583	-3.04184	2.894594
C	-0.5102	-2.10347	2.135297	1.323428	-1.83634	2.255182
C	-1.56944	1.490596	2.13387	-2.30772	-0.26435	2.215319
C	-2.04467	2.656694	2.759558	-3.52879	0.04254	2.840618
C	-1.67685	3.895489	2.267861	-4.32008	1.041306	2.307274
C	-0.83014	3.963016	1.138544	-3.89037	1.726285	1.147405
C	-0.40827	2.737243	0.5731	-2.64674	1.342539	0.583898
C	-0.37733	5.190271	0.544429	-4.65162	2.779327	0.537194
H	1.362771	1.33597	2.517405	-0.08091	1.910285	2.629705
H	3.564279	1.044098	3.631031	1.441361	3.547037	3.741858
H	5.177068	-0.6488	2.743577	3.727799	3.907826	2.793523
H	5.661067	-2.45438	0.98481	5.432869	3.332177	1.02546
H	4.913015	-3.73387	-0.98202	6.047505	2.043479	-0.98516

H	3.101706	-4.19855	-2.74014	5.417955	0.368749	-2.76407
H	0.83507	-3.62396	-3.62717	3.69087	-1.16772	-3.72133
H	-0.4985	-1.84767	-2.51446	1.463231	-1.32225	-2.60942
H	1.851521	0.488746	-2.51278	0.410006	1.862513	-2.63263
H	2.727186	2.530776	-3.62407	-0.80776	3.735155	-3.74792
H	2.092959	4.781755	-2.73781	-2.99688	4.487197	-2.79954
H	0.783516	6.119547	-0.98197	-4.77432	4.218462	-1.02955
H	-1.34506	1.353836	-2.5174	-1.79296	-0.58271	-2.65678
H	-3.55021	1.091012	-3.63104	-2.75181	-2.58202	-3.79542
H	-5.18519	-0.58046	-2.74359	-2.32017	-4.84996	-2.82935
H	-5.69297	-2.3795	-0.98482	-1.23818	-6.23964	-1.02392
H	-4.96188	-3.66873	0.982032	0.128363	-6.36005	1.025252
H	-3.15688	-4.15722	2.740179	1.438163	-5.18113	2.829717
H	-0.88287	-3.61255	3.627231	2.261354	-3.02376	3.794762
H	0.474021	-1.85401	2.514513	1.666858	-0.88754	2.656259
H	-1.84494	0.513222	2.512755	-1.66509	-1.04334	2.614669
H	-2.69351	2.566671	3.624027	-3.83146	-0.50342	3.727604
H	-2.02954	4.809053	2.737766	-5.26795	1.306096	2.767358
H	-0.70249	6.129388	0.981924	-5.60042	3.060068	0.98459

S10 Simulated difference spectra of the $^5T_{2g}$ state under various tetragonal distortions

The ligand cage of the Frank-Condon $^5T_{2g}$ state may be subject to tetragonal geometric distortions in addition to the fully symmetric compression described in the main paper. These tetragonal distortions split the previously degenerate e_g and t_{2g} orbitals. Figure S11 shows the difference spectra (distorted minus equilibrium where 10Dq = 0.6 eV) simulated for several combinations of e_g and/or t_{2g} splittings that may be achieved in a MLCT-^{3}T-$^5T_{2g}$ transition. When calculating the energy-dependent oscillation amplitude, the Auger linewidth is restricted to be within ±0.3 eV from a linear fit to the transition energy vs linewidth in order to suppress spurious variations in the computed linewidth.

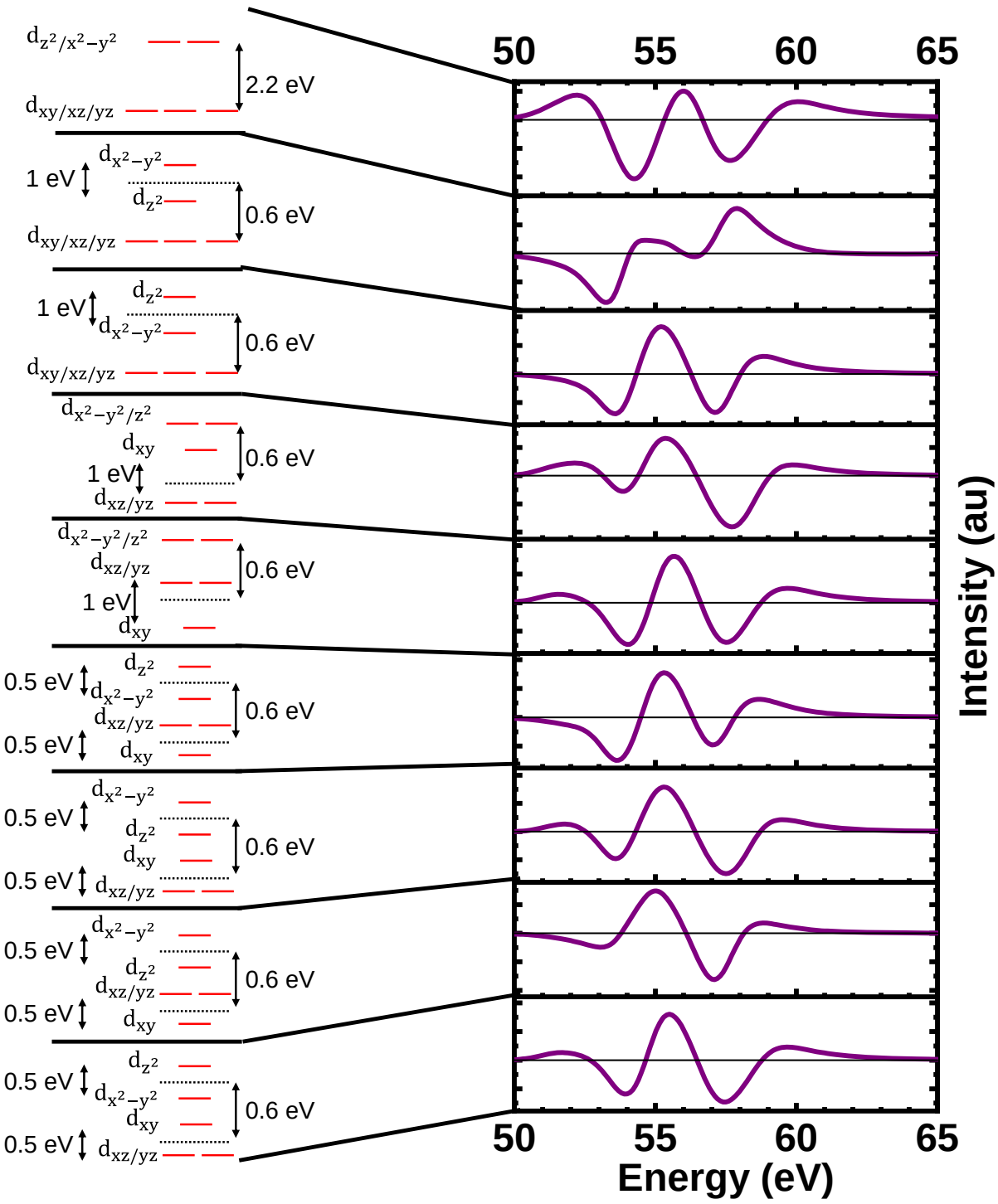

Figure S11 Simulated difference spectra of $^5T_{2g}$ under various tetragonal distortions

References

(1) Lin, M.-F.; Verkamp, M. A.; Leveillee, J.; Ryland, E. S.; Benke, K.; Zhang, K.; Weninger, C.; Shen, X.; Li, R.; Fritz, D.; Bergmann, U.; Wang, X.; Schleife, A.; Vura-Weis, J. Carrier-Specific Femtosecond XUV Transient Absorption of PbI_2 Reveals Ultrafast Nonradiative Recombination. *J. Phys. Chem. C* **2017**, *121* (50), 27886–27893.

(2) Warner, B.; Oberg, J. C.; Gill, T. G.; El Hallak, F.; Hirjibehedin, C. F.; Serri, M.; Heutz, S.; Arrio, M.-A.; Sainctavit, P.; Mannini, M.; Poneti, G.; Sessoli, R.; Rosa, P. Temperature- and Light-Induced Spin Crossover Observed by X-Ray Spectroscopy on Isolated Fe(II) Complexes on Gold. *J. Phys. Chem. Lett.* **2013**, *4* (9), 1546–1552.

(3) Ellingsworth, E. C. C.; Turner, B.; Szulczewski, G. Thermal Conversion of [Fe(Phen)3](SCN)2 Thin Films into the Spin Crossover Complex Fe(Phen)2(NCS)2. *RSC Adv.* **2013**, *3* (11), 3745–3754.

(4) Nitzan, A. *Chemical Dynamics in Condensed Phases*; Oxford University Press: New York, 2006.

(5) Golub, G. H.; Pereyra, V. The Differentiation of Pseudo-Inverses and Nonlinear Least Squares Problems Whose Variables Separate. *SIAM J. Numer. Anal.* **1973**, *10* (2), 413–432.

(6) Frisch, M. J.; Trucks, G. W.; Schlegel, H. B.; Scuseria, G. E.; Robb, M. A.; Cheeseman, J. R.; Scalmani, G.; Barone, V.; Mennucci, B.; Petersson, G. A.; Nakatsuji, H.; Caricato, M.; Li, X.; Hratchian, H. P.; Izmaylov, A. F.; Bloino, J.; Zheng, G.; Sonnenberg, J. L.; Hada, M.; Ehara, M.; Toyota, K.; Fukuda, R.; Hasegawa, J.; Ishida, M.; Nakajima, T.; Honda, Y.; Kitao, O.; Nakai, H.; Vreven, T.; Montgomery, J. A.; Peralta, J. E.; Ogliaro, F.; Bearpark, M.; Heyd, J. J.; Brothers, E.; Kudin, K. N.; Staroverov, V. N.; Keith, T.; Kobayashi, R.; Normand, J.; Raghavachari, K.; Rendell, A.; Burant, J. C.; Iyengar, S. S.; Tomasi, J.; Cossi, M.; Rega, N.; Millam, J. M.; Klene, M.; Knox, J. E.; Cross, J. B.; Bakken, V.; Adamo, C.; Jaramillo, J.; Gomperts, R.; Stratmann, R. E.; Yazyev, O.; Austin, A. J.; Cammi, R.; Pomelli, C.; Ochterski, J. W.; Martin, R. L.; Morokuma, K.; Zakrzewski, V. G.; Voth, G. A.; Salvador, P.; Dannenberg, J. J.; Dapprich, S.; Daniels, A. D.; Farkas, O.; Foresman, J. B.; Ortiz, J. V.; Cioslowski, J.; Fox, D. J. *Gaussian 09, Revision D.01*; Gaussian, Inc.: Wallingford CT, 2013.